Blocking gephyrin phosphorylation or microglia BDNF signaling prevents synapse loss and reduces infarct volume after ischemia.

Teresa Cramer[1]*, Raminder Gill[2]*, Zahra S Thirouin[1]*, Markus Vaas[1]*, Suchita Sampath[1], Sara B. Noya[1], Philip K.-Y. Chang[2], Peiyou Wu[2], Philip A Barker[3], Rosa C. Paolicelli[4], Jan Klohs[5], Shiva K. Tyagarajan[1]#, R. Anne McKinney[2]#

1. Institute of Pharmacology and Toxicology, University of Zurich, Winterthurerstrasse 190, CH 8057, Switzerland

2. Department of Pharmacology and Therapeutics, McGill University, 3649 Prom. Sir-William-Osler, Montreal, QC, H3G 0B1, Canada

3. Department of Biology, University of British Columbia, 3187 University Way, ASC 413 Kelowna, BC, V1V 1V7, Canada

4. Department of Biomedical Sciences, University of Lausanne, Rue du Bugnon 7 - CH-1005 Lausanne

5. Institute for Biomedical Engineering, University of Zurich and ETH Zurich, Wolfgang-Pauli-Strasse 27, CH 8093, Switzerland

* equal contribution

 # Co-senior and co-correspondence to:

anne.mckinney@mcgill.ca

tyagarajan@pharma.uzh.ch

Abstract:

Microglia interact with neurons to facilitate synapse plasticity; however, signal transducers between microglia and neuron remain unknown. Here, using *in vitro* organotypic hippocampal slice cultures and transient MCAO in genetically-engineered mice *in vivo*, we report that at 24 h post-ischemia microglia release BDNF to downregulate glutamatergic and GABAergic synaptic transmission within the penumbra area. Analysis of the CA1 hippocampal formation *in vitro* shows that proBDNF and mBDNF downregulate dendritic spine and gephyrin scaffold stability through $p75^{NTR}$ and TrkB receptors respectively. Post-MCAO, we report that in the penumbra and in the corresponding contralateral hemisphere similar neuroplasticity occur through microglia activation and gephyrin phosphorylation at Ser268, Ser270. Targeted deletion of the *Bdnf* gene in microglia or *Gphn*S268A/S270A (phospho-null) point-mutations protect against ischemic brain damage, neuroinflamation and synapse downregulation post-MCAO. Collectively, we report a new unanticipated role for gephyrin phosphorylation in inflammation and microglia activation for neuroprotective plasticity after transient ischemia.

Introduction:

Stroke is a major cause of death and long-term disability worldwide. Therapeutic approaches to CNS ischemia developed in the laboratory have focused on mechanisms contributing to ischemic damage, namely excitotoxicity, oxidative stress and inflammation (Brouns and Deyn, 2009; Lakhan et al., 2009). Clinical intervention targeting glutamate receptors (Albers et al., 2001), GABA receptors (Lyden et al., 2000), calcium channels (Zhang et al., 2019), sodium channels (Gibson et al., 2010)and free radicals (Shuaib et al., 2007)have failed during clinical trials. However, the brain has developed inherent mechanism(s) for self-preservation, and gaining insights into these protective measures may provide a way forward to counteract ischemic brain injury.

In the ischemic core, rapid cell death occurs: However, in the penumbra or peri-infarct area, region with constrained blood flow with partially preserved energy metabolism neurons survive, propagating neuronal depolarization in combination with impairment of glia function causes increased extracellular concentration of ions and neurotransmitters, and induces functional disturbances (Campbell et al., 2019). Morphologically, both dendritic spines of excitatory neurons (Zhang et al., 2005) and GABAergic synapses (Alicke and Schwartz-Bloom, 2002) are reduced. Interestingly, the neurotrophin Brain-derived neurotrophic factor (BDNF) can decrease ischemic core volume and improve neurological outcome after experimental stroke either upon overexpression *in vivo* using genetic methods (Yu et al., 2013) or upon exogenous supply (Scha□bitz et al., 2007). Likewise, inhibition of BDNF exacerbates ischemic damage. Glutamatergic neurotransmission induces BDNF expression (Gottlieb et al., 2013). BDNF is expressed as a proprotein, proBDNF, and is subsequently processed to its mature form mBDNF (Adachi et al., 2014). proBDNF, binds to $p75^{NTR}$ receptor and negatively regulates dendritic

spines through Rho/Rac activation (Yang et al., 2014). mBDNF signals through TrkB receptors to enhance excitatory neurotransmission (Tanaka et al., 2008). mBDNF can also bind to $p75^{NTR}$ receptors, albeit with much lower affinity (Kraemer et al., 2014). At GABAergic synapses, mBDNF induces internalization of $GABA_A$ receptors (Brünig et al., 2001) and downregulation of the main scaffolding protein gephyrin (Mou et al., 2013), thereby reducing GABAergic transmission in principal cells.

Ischemia also activates inflammatory pathways that subsequently recruit leukocytes to the injured brain (Wood, 2019). There is evidence for immune cells contributing to both neuroprotection and programmed cell death (Schafer and Stevens, 2015), suggesting that the temporal window of inflammation might determine cell survival or death. Such deleterious signaling events must be counteracted to mitigate tissue damage and re-establish homeostasis. Microglia are the resident immune cells in the central nervous system (CNS) and primary responders during defense. They clear cellular debris as part of the tissue repair and wound healing processes (Lenz and Nelson, 2018; Lenz et al., 2013). In recent years, an essential role for microglia in synapse pruning during postnatal brain development has emerged (Reemst et al., 2016). Microglia activation can be triggered by acute insult, causing process elongation and increased expression of marker proteins like IBA1 and CD11b (Fumagalli et al., 2013). Microglia activation can protect the brain, albeit precise cellular and molecular mechanisms for microglia influenced neuroprotection remain unclear. Microglia processes can directly sense synaptic activity (Li et al., 2012), and can regulate neuronal calcium load and functional connectivity through neuronal mitochondrial function and P2Y12 receptor activation on contacting microglia (Cserép et al., 2019). Subsequent LPS-induced activation of downstream calcium-calmodulin-dependent kinase (CaMKIV), cyclic AMP response element binding protein

(CREB) phosphorylation and BDNF protein increase facilitate neuron survival after cortical injury (Chen et al., 2012). It is conceivable that such mechanisms might also be neuroprotective after CNS ischemia.

BDNF administered either intravenously (Schabitz et al., 2007), with viral vectors (Yu et al., 2013), or by addition of the bioactive high-affinity TrkB agonist, 7,8-dihydroxyflavone, can protect neurons from apoptosis and decrease infarct volumes in animal model of stroke (Jang et al., 2010). These findings suggest that elevated BDNF is beneficial for recovery after stroke. However, the source of BDNF after ischemia and the mechanisms underlying the beneficial effect of BDNF remain unclear. Here, we set out to assess the self-preservation mechanism(s) that counteract ischemic brain damage and enable tissue repair and neural network reorganization. Using organotypic hippocampal slice cultures and the oxygen-glucose deprivation (OGD) model of ischemia, we report that within first 90 min post-ischemia, proBDNF via $p75^{NTR}$ disrupts glutamatergic, and mBDNF via TrkB disrupts GABAergic neurotransmission. We uncover that ERK1/2 and GSK3β pathways downstream of TrkB phosphorylate gephyrin at Ser 268 and Ser 270 residues resulting in GABAergic synapse loss. Using transient middle cerebral artery occlusion (MCAO) in wildtype and genetically-engineered mice, we uncover a central role for BDNF derived from microglia in influencing gephyrin phosphorylation downstream of TrkB receptor signaling. Using pharmacological depletion of microglia, CRISPR/Cas9 generated *Gphn*S268A/S270A mutant mouse, and *Bdnf* gene deletion from microglia, we demonstrate each time reduced inflammation and enhanced neuroplasticity after MCAO. Collectively, these observations unravel BDNF as the signal transducer between microglia and neurons, in turn activating ERK1/2 and GSK3b pathways downstream to influence gephyrin scaffold stability at GABAergic synaptic sites. Plasticity adaptations at GABAergic and

glutamatergic synapses influence microglia activation and provide neuroprotection after transient ischemia.

Results:

OGD causes glutamatergic and GABAergic synapse downregulation

To understand the mechanisms of BDNF action in ischemia we started with the *in vitro* model of ischemia, OGD, in organotypic hippocampal slice cultures from transgenic mice that express myristoylated GFP in a subset of CA1 neurons (Gill et al., 2013) and studied synaptic changes in CA1 area after OGD (4 min) and recovery at 90 min and 24 h. We confirmed the effects of OGD by measuring hypoxia-inducible factor 1 α (HIF1α) expression (Bergeron et al., 1999) and found 1.5-fold increase in HIF1α expression in area CA1 90 min after OGD. First, we determined glutamatergic synapse alterations after OGD by measuring changes in dendritic spines (McKinney, 2009). We observed an overall reduction in spine density at both 90 min and 24 h following OGD compared to control cultures (Fig. 1a, b; Supp. Fig. 1a) specifically affecting mushroom and long-thin subtype of spines (Fig. 1b).

Next, we evaluated OGD-induced changes at GABAergic synapses in area CA1 at 90 min and 24 h following OGD. We immunostained for VGAT and gephyrin, and saw a significant overall downregulation in gephyrin cluster density 90 min following OGD compared to control (Fig. 1c-e) in the stratum radiatum. However, after 24 h gephyrin cluster density remained significantly reduced, while cluster volume had recovered to baseline (Suppl. Fig. 1a´-a´´).

To determine whether these morphological changes were accompanied by a functional deficit, we recorded AMPA-mediated miniature excitatory postsynaptic currents (mEPSCs) from CA1 pyramidal neurons within 24 h after OGD (Fig. 1f-f'; Suppl. Fig. 1b-b''). We found that the input resistance and resting membrane potential of CA1 hippocampal pyramidal cells in OGD

and sister untreated cells were similar, suggesting that OGD does not impact receptor open probability or intracellular chloride concentration. However, we found a significant decrease in the mEPSC amplitude in OGD-treated slices compared to control (Fig. 1f, Suppl. Fig. 1b). Similarly, the inter-event-interval (IEI) of mEPSC of OGD cells were increased compared to control (Fig. 1f'; Suppl. Fig. 1b'). Taken together, dendritic spine loss is mirrored by functional loss of excitatory synapses 24 h after OGD. Subsequently, to determine whether inhibitory circuitry was also affected we recorded $GABA_A$-mediated miniature inhibitory postsynaptic current (mIPSC) within 24 h of OGD induction. mIPSC analysis showed no observable changes in the amplitude of mIPSC after OGD compared to control slices (Fig. 1g; Suppl. Fig. 1c). However, a significant increase in the IEI in OGD-treated slices was observed (Fig. 1g'; Suppl. Fig. 1c'). These functional data recapitulate the morphological observations that inhibitory synapse loss after OGD does not recover, but total $GABA_A$Rs at synaptic sites within the existing synapses recover at 24 h after OGD.

Scavenging BDNF after OGD using TrkB-Fc rescues OGD-induced synapse deficit

As BDNF is upregulated after ischemia (Béjot et al., 2010; Lai et al., 2018), we assessed whether BDNF signaling contributed to synapse loss on CA1 pyramidal neurons after OGD. We scavenged proBDNF and mBDNF using chimeric TrkB-Fc (10µg/mL) and exposed organotypic hippocampal slices to 4 min OGD. Dendritic spine quantification in CA1 pyramidal neurons showed prevention of total spine density loss caused by OGD in TrkB-Fc treated cultures in comparison to untreated cultures (Fig. 2a, b). Specifically, the OGD-induced decrease in mushroom and long-thin subtype of dendritic spines was prevented by TrkB-Fc (Fig. 2a, b). We next assessed whether TrkB-Fc treatment also protects GABAergic synapses by quantifying for

post-synaptic gephyrin clustering in OGD cultures that were either treated with TrkB-Fc or not. These data showed a consistent protection of gephyrin clusters by TrkB-Fc (Fig. 2c-e). Importantly, TrkB-Fc caused no detectable effect in control cultures (not exposed to OGD).

To determine whether morphological synapse protection is recapitulated functionally, we recorded AMPA-mediated mEPSC from CA1 pyramidal neurons from all groups. We found that the OGD-induced reduction of mEPSC amplitudes 24 h following OGD was prevented by TrkB-Fc treatment, being comparable to treated and untreated controls (Fig. 2f; Suppl. Fig. 1d-d''). Similarly, increase in IEI was also prevented by TrkB-Fc treatment as seen 24 h after the induction of OGD, with values similar to treated and untreated control slices (Fig. 2f'; Suppl. Fig. 1d'), indicating that the reduced occurrence of mEPSC after OGD was due to BDNF signaling.

We then recorded $GABA_A$-mediated mIPSC from CA1 pyramidal neurons from all groups. We found that mIPSC amplitudes were comparable in all groups (Fig. 2g, g'; Suppl. Fig. 1e). The previously observed increase in IEI caused by OGD was prevented with TrkB-Fc treatment to control levels (Fig. 2g'; Suppl. Fig. 1f'), confirming that the OGD-induced decrease in glutamatergic and GABAergic synapse loss is mediated by BDNF.

proBDNF and mBDNF signal via p75^{NTR} and TrkB receptors to induce glutamatergic and GABAergic synapse loss respectively after ischemia

We next investigated the molecular pathways involving BDNF-mediated synapse loss at 90 min post OGD in organotypic hippocampal slice cultures. To specifically investigate the contribution of proBDNF on OGD-induced dendritic spine loss, we used blocking antibodies to either inhibit proBDNF or $p75^{NTR}$. Pre-treatment of OGD slices with either anti-proBDNF or anti-$p75^{NTR}$

antibodies prevented OGD-induced dendritic spine loss (Fig. 3a-c). Additionally, treatment of OGD slices with anti-proBDNF or anti-$p75^{NTR}$ antibody did not prevent gephyrin cluster loss after OGD (Fig. 3d). These findings indicate that pro-BDNF signaling through $p75^{NTR}$ to specifically induces excitatory synapses loss following OGD.

We next investigated the role of mBDNF in OGD-induced synapse loss. For this we pretreated cultures with anti-mBDNF (N-9, a function blocking antibody) prior to OGD and then quantified the dendritic spines; control sister cultures were processed simultaneously with and without anti-mBDNF treatment. The data revealed a significant downregulation of total dendritic spines in both OGD and anti-mBDNF pretreated OGD slices, compared to control and cultures pretreated with anti-mBDNF (Fig. 3e-f). Similar to our earlier observations, only the mushroom and long-thin subtype of dendritic spines were downregulated 90 min following OGD with or without anti-mBDNF treatment (Fig. 3g). This data suggested to us that mBDNF was not mediating excitatory synapse loss after OGD. In contrast, anti-mBDNF treatment was sufficient to prevent the reduction of gephyrin cluster density compared to OGD-only slices (Fig. 3h). Reduction of gephyrin cluster volume was also prevented in the presence of anti-mBDNF antibody compared to OGD slices (Fig. 3i). Our results show that mBDNF acts specifically on GABAergic synapses after OGD.

Blocking ERK1/2 and GSK3β pathways protects gephyrin, but not dendritic spine loss

mBDNF binds with high-affinity to TrkB receptors. It is also known that ERK1/2 and GSK3β pathways are activated downstream of TrkB (Mohammadi et al., 2018). Therefore, we determined whether ERK1/2 and GSK3β signaling cascades downstream of TrkB were activated after OGD to mediate gephyrin cluster reduction at GABAergic terminals. We pretreated slices

with pharmacological inhibitors of GSK3β (25 μM GSK3β-IX) and MEK (30 μM PD98059) to prevent activation of these kinases before OGD. Control treated and untreated cultures served for comparative analysis. As expected, inhibiting ERK1/2 and GSK3β pathways did not prevent dendritic spine loss in OGD treated cultures (Fig. 4a, b). Specifically, the mushroom and stubby dendritic spines that were most affected by OGD could not be rescued with ERK1/2 and GSK3β blockade (Fig. 4b). However, at GABAergic synapses gephyrin cluster loss was prevented after OGD in slices pretreated with GSK3β-IX and PD98059, compared to untreated OGD slices (Fig. 4a, c, d). Interestingly, treating OGD cultures with PD98059 alone successfully rescued the gephyrin cluster volume but not the cluster density. On the other hand, GSK3β-IX treatment alone was successful in partially recovering gephyrin cluster density after OGD.

Previously, we have reported that GSK3β phosphorylates gephyrin on serine 270 (ser270) to negatively regulate the number of gephyrin clusters (Tyagarajan et al., 2011), and ERK1/2 phosphorylates gephyrin at serine 268 (ser268) to negatively regulate the size of gephyrin clusters (Tyagarajan et al., 2013). In order to determine whether phosphorylation of these serine residues were important for OGD-induced gephyrin downregulation, we used biolistic transfection of GFP-tagged gephyrin where serines 268 and 270 were mutated to alanines ($gephyrin_{S268A/S270A}$) into CA1 pyramidal neurons and assessed whether this gephyrin mutant is insensitive to mBDNF-mediated TrkB signaling after OGD. Our analysis showed that $gephyrin_{S268A/S270A}$ mutant is resistant to OGD compared to wildtype gephyrin ($gephyrin_{WT}$) (Fig. 4e, f, h, i). Transgene expression of $gephyrin_{S268A/S270A}$ mutant could not prevent dendritic spine loss after OGD, which is consistent with the data using pharmacological inhibitors (Fig. 4g). Overall, our results identify gephyrin S268 and S270 phosphorylation downstream of TrkB as a determinant for GABAergic synapse loss after OGD.

The MCAO model *in vivo* recapitulates OGD-induced synapse loss at 24 h post ischemia

In order to confirm our *in vitro* OGD results, we employed the *in vivo* MCAO technique, in which uses an intraluminal filament is used to obturate the middle cerebral artery and cause transient ischemia in fronto-parietal cortex and striatum (Morris et al., 2016) and assayed for glutamatergic and GABAergic synapse loss 24 h later. This technique is the most extensively used model in rodents as it produces reproducible infarct (core and penumbra) mimicking human ischemic strokes. The penumbra surrounding the core is the site for synaptic plasticity and circuit adaptations following cell death in the core. Structural and functional changes within the penumbra have been observed in patients after 3 months following an anterior ischemic stroke (Yassi et al., 2015). The cell death within the ischemic core renders the tissue fragile for morphology or functional analysis; hence, we restricted our analysis to the penumbra.

We used immunohistochemical staining to assess glutamatergic and GABAergic synapse changes within the penumbra and in the corresponding area contralaterally as comparison. For glutamatergic synapse labeling we chose VGLUT1 and PSD95 (Fig. 5a, b, c), while for GABAergic synapse labeling we chose GAD65/67; $GABA_AR$ γ2 for synaptic receptors and $GABA_AR$ α5 for extrasynaptic receptors (Fig. 5a, d, e, f). Analysis of parietal cortex layer 2/3 (L2/3) 24 h after MCAO did not show any observable loss of PSD95 (Fig. 5c). This result is consistent with the report that, under ischemic conditions, nNOS interacts with PSD95 to stabilize it at the cell membrane (Zhou et al., 2010). Analysis for VGLUT1-positive terminals showed a significant reduction in presynaptic sites in both ipsi- and contra-lateral hemispheres (Fig. 5b).

At GABAergic synapses, we saw a significant reduction in GAD65/67 terminals, γ2 subunit-containing synaptic $GABA_ARs$ and α5 subunit-containing extrasynaptic $GABA_ARs$ (Fig. 5d-f). We could not morphologically assess for α1 and α2 subunit-containing $GABA_ARs$ in MCAO tissue due to antibody limitation. Therefore, we used Western blot (WB) to examine the expression level of α1 and α2 subunits in control and MCAO tissue from both ipsi- and contra-lateral hemispheres of parietal cortex L2/3. We found a significant reduction in α1 and α2 $GABA_AR$ subunit expression after MCAO (Suppl. Fig 2a, b). Overall, our analysis confirms that both ipsi- and contra-lateral hemispheres decrease protein expression of important glutamatergic and GABAergic synaptic markers. Therefore, reduced excitatory and inhibitory synapse markers *in vivo* recapitulate *in vitro* OGD results showing impaired glutamatergic and GABAergic synaptic transmission loss.

Synapse loss after MCAO is attenuated in GphnS268A/S270A point mutant mice

Blocking effector kinases downstream of TrkB *in vitro* OGD experiments effectively rescued GABAergic synapse loss (Fig. 4c-d) and transgene expression of gephyrin S268A/S270A mutant insensitive to ERK1/2 and GSK3β kinases prevented gephyrin cluster loss after OGD (Fig. 4h-i). Hence, we assessed ERK1/2 and GSK3β kinase activation levels 24 h after MCAO in fronto-parietal cortex ipsi- and contralaterally in WT mice. WB analysis for ERK1/2 and its phosphorylated form showed unchanged ERK1/2 levels but significantly increased levels of phosphorylated ERK1/2 in the ipsi- but not the contra-lateral hemisphere at 24 h after MCAO (Suppl. Fig. 3a, b). WB analysis for GSK3β showed increased kinase expression in the contra-lateral hemisphere but not the ipsi-lateral hemisphere at 24 h after MCAO (Suppl. Fig. 3a, c). Gephyrin expression level and its phosphorylation at Ser 268 and Ser 270 sites changed at 24 h

after MCAO (Suppl. Fig. 3d-g). The WB quantification confirmed that total gephyrin protein levels significantly decrease at 24 h post MCAO (Suppl. Fig. 3d, e). Consistent with our observation of elevated ERK1/2 activation on the ipsi-lateral hemisphere, we observed significantly higher S268 phosphorylation on gephyrin (Suppl. Fig. 3f). Similarly, higher GSK3β levels in the contra-lateral hemisphere correlated with significantly higher gephyrin S270 phosphorylation (Suppl. Fig. 3g). These observations are consistent with our *in vitro* OGD data, and further confirm a role for ERK1/2 and GSK3β pathways in directly phosphorylating gephyrin to regulate protein stability after MCAO.

To obtain a more direct confirmation for the central role of gephyrin phosphorylation in synapse alterations 24 h post-MCAO, we generated a *Gphn*S268A/S270A global point mutant mouse line using CRISPR/Cas9 (Cyagen, USA). These mice breed with Mendelian ratios and show no abnormalities in brain size and body weight compared to WT littermates. We performed MCAO in *Gphn*S268A/S270A mutant mice and compared synapse plasticity changes in the parietal cortex L2/3 with sham *Gphn*S268A/S270A littermates. We analysed for changes in glutamatergic and GABAergic synaptic markers using immunohistochemical analysis 24 h post-MCAO (Fig. 6). In the *Gphn*S268A/S270A mutant mice, we observed stabilization of excitatory VGLUT1-positive terminals on both ipsi- and contralateral hemispheres 24 h post MCAO (Fig. 6a, b, b'). Interestingly, PSD95 cluster density was also unchanged in the ipsi- and the contra-lateral hemispheres (Fig. 6b'). Analysis of GABAergic synaptic markers showed a significant increase in the GAD65/67 puncta density in both ipsi- and contra-lateral hemispheres (Fig. 6c). Significantly, we did not observe any reduction in γ2- and α5-containing $GABA_A$Rs in *Gphn*268/S270A mutant mice 24 h post MCAO (Fig. 6 c'-c''). Consistent with observed synaptic marker changes, WB analysis for the α1 and α2 subunits in *Gphn*268/S270A mutant

mice showed no alterations for these two major $GABA_AR$ subunits 24 h following MCAO (Suppl. Fig. 2c-d). Taken together, our results identify ERK1/2 and GSK3β as downstream effectors that critically influence gephyrin scaffold stability along with glutamatergic and GABAergic synapse integrity post-MCAO.

GphnS268A/S270A mutation or Bdnf deletion from microglia reduce brain damage after MCAO

Next we wanted to assess whether the absence of synaptic changes at 24 h post-MCAO in *Gphn*S268A/S270A mutant mice is due to tissue preservation. BDNF has been shown to play the role of pro-survival factor, including microglia activation *in vivo* (Jiang et al., 2010). While the source of BDNF in conditions of ischemia remains unclear, there is evidence to suggest that neuronal activity-dependent exocytosis and/or release from microglia can contibute to conditions of specific brain pathology (Gomes et al., 2013). To assess whether microglia released BDNF during neuroinflamation, we used CX3CR1-ERT2Cre mice specifically expressing tamoxifen-inducible Cre recombinase in microglia cells and generated $BDNF^{Tg/Tg}$ / $CX3CR1^{CreERT2/+}$ double transgene mouse line, thereby preventing *Bdnf* expression selectively in microglia. We wondered whether ablating *Bdnf* from microglia cells specifically would also contribute to tissue preservation after MCAO. To test this, we performed MCAO in *Gphn*S268A/S270A mutant mice or $BDNF^{Tg/Tg}$ / $CX3CR1^{CreERT2/+}$ double transgene mice (Fig. 7a, b). We used cresyl violet staining to measure the infarct volume across brain sections 24 h following MCAO. Quantification confirmed that in both *Gphn*S268A/S270A mutant mice and $BDNF^{Tg/Tg}$ / $CX3CR1^{CreERT2/+}$ double transgene mice the ischemic tissue damage was significantly reduced as compared to WT mice.

GphnS268A/S270A mice prevents microglia activation and BDNF increase after MCAO

The similarities observed so far between OGD *in vitro* and MCAO *in vivo* suggest the contribution of similar mechanisms. However, *in vivo*, inflammatory processes play a key role in tissue damage and repair. Therefore, prior to investigating a possible role of BDNF as mediator of synapse loss after MCAO *in vivo*, we first examined the density of resident glial cells, namely astrocytes and microglia at baseline in the brain of WT, *Gphn*S268A/S270A mutant mice, $BDNF^{wt/wt}$ / $CX3CR1^{CreERT2+/-}$ and $BDNF^{Tg/Tg}$ / $CX3CR1^{CreERT2+/-}$ mice (Suppl. Fig. 4). Quantification for Glial fibrillary acidic protein (GFAP) positive soma for astrocyte density showed no difference between WT, *Gphn*S268A/S270A mutant mice, $BDNF^{wt/wt}$ / $CX3CR1^{CreERT2/+}$ and $BDNF^{Tg/Tg}$ / $CX3CR1^{CreERT2+/-}$ (Suppl. Fig. 4a'). The quantification for ionized calcium-binding adaptor protein-1 (IBA-1) positive microglia confirmed no difference in cell density between WT, *Gphn*S268A/S270A mutant mice, $BDNF^{wt/wt}$ / $CX3CR1^{CreERT2/+}$ and $BDNF^{Tg/Tg}$ / $CX3CR1^{CreERT2+/-}$ (Suppl. Fig. 4b').

We next assessed the activation of astrocytes and microglia in 24 h post-MCAO tissue. In response to inflammation, astrocytes and microglia acquire properties for reactive species generation and inflammatory cytokine production, and are therefore thought to be principal drivers of pro-inflammatory responses (Buscemi et al., 2019; Wei et al., 2011). Microglia have further been implicated in the rapid engulfment and clearance of synapses following brain pathology (Paolicelli et al., 2017). Hence, we compared inflammatory responses in the penumbra of WT and *Gphn*S268A/S270A mutant mice 24 h following MCAO. We stained for activation-state markers of astrocytes and microglial cells as biomarkers of inflammation.

It has been reported that macrophages infiltrate into the CNS only at day 4 following MCAO (Rajan et al., 2018); therefore, IBA-1 positive cells are likely to be resident microglial

cells. The hyperthrophy of microglia and astrocytes after brain injury has been extensively reported in literature. To confirm inflamation and microglia and astrocyte activation status at 24 h post-MCAO we stained for IBA-1 and CD11b for microglial cells, and GFAP for astrocytes respectively (Fig. 7c). In WT mice, we found significant shortening of microglial process length identified via IBA1 staining in the ipsi-lateral hemisphere. In the contra-lateral hemisphere we observed a significant increase in the IBA1 process length (Fig. 7d,f). These observations are consistent with the literature (Fumagalli et al., 2013) In our MCAO tissue, we observed significant increase in CD11b intensity in the ipsi-, but not the contra-lateral hemisphere (fig. 7d'). Consistent with the IBA1 staining in microglial cells, GFAP staining showed retracted processes in the ipsi-lateral hemisphere and extended process length in the contra-lateral hemisphere (Fig. 7e,f).

If indeed gephyrin scaffold stabilization leads to reduced neuroinflammation, we anticipated less activation of microglia and astrocytes in *Gphn*S268A/S270A mutant mice after MCAO. Indeed, microglia processes were not hypertrophic after MCAO in the *Gphn*S268A/S270A mutant mice (Fig. 7g, h, j). However, in the contra-lateral hemisphere microglia exhibited a ramified surveillance state showing that gephyrin scaffold stabilization could not completely block the immune surveillance from getting active. Analysis for changes in CD11b in *Gphn*S268A/S270A mutant mice showed consistent reduction of CD11b intensity in the ipsi-lateral hemisphere after MCAO (Fig. 7h'). Examination of changes in astrocyte process length using GFAP showed only a modest yet significant reduction in the astrocyte process length in the ipsi-lateral hemisphere (Fig. 7i). Similarly, analysis of astrocyte process length in the contra-lateral hemisphere also showed a small yet significant increase. Overall, our data

shows that in *Gphn*268/S270A mutant mice, the mutation selectively blocks MCAO-induced microglia activation.

Activated microglia induce synapse loss after MCAO

While it is well established that BDNF levels increase after cerebral ischemia, the source of BDNF after stroke remains unclear. Given that microglia defects in *Gphn*S268A/S270A mutant mice were more prominent, we wondered whether microglia contributed to BDNF signaling after stroke. As a first step towards testing this hypothesis, we depleted microglia from the brain using the pharmacological inhibitor PLX5622 that targets colony stimulating factor 1 receptor (CSF-1R) phosphorylation in microglia (Plexxikon Inc. Berkeley, CA 94710). It has been reported that prolonged administration of this drug (1 week) in a formulated chow diet depletes 90% of the microglia from rodent brain (Elmore et al., 2018; Spangenberg et al., 2016). Replacing the mice on regular diet repopulates microglia cells within 5-7 days. No adverse changes to the synapse structure and function, or transcriptional changes have been reported after PLX5622 chow administration (Elmore et al., 2014). We confirmed the loss of microglia after PLX5622 chow administration after 7 days. We subject WT mice to MCAO after treatment with either PLX5622 formulated chow or control chow. We first assessed whether microglia depletion affected astrocyte morphology in the penumbra of ipsi-lateral hemisphere and corresponding area in the contra-lateral hemisphere at 24 h post-MCAO. To measure astrocyte changes we stained for GFAP and measured process lengths. Quantification showed a significant reduction in GFAP process length similar to WT animals in the ipsi-lateral side, but no extension of the processes could be observed in the contra-lateral side (Suppl. Fig. 5a, b, c). These results confirmed that astrocyte activation is not dependent on microglia.

Next, we analyzed for synapse alterations at 24 h post MCAO in WT mice either treated with PLX5622 formulated chow or control chow. We stained for synaptic markers and found no significant differences in either glutamatergic synaptic markers (VGLUT1, PSD-95) or GABAergic synaptic markers (GA65/67, α5 and γ2 $GABA_AR$s) between the groups (Suppl. Fig. 4d-g). WB analysis to assess α1 or α2 $GABA_AR$ subunit expression showed no changes at 24 h post-MCAO in mice administered with PLX5622 (Suppl. Fig. 2e, f). In addition, WB analysis to assess total gephyrin or changes in gephyrin phosphorylation at S268 and S270 residues showed no changes (Suppl. Fig. 3h-k). These findings point to the critical role of microglia in mediating synapse loss after MCAO, most likely down stream of gephyrin phosphorylation.

Microglia release BDNF after MCAO to induce synapse loss

BDNF has been shown to play a critical role in the activation of microglia *in vitro,* and increase in BDNF has been tightly linked to pro-inflammation responses (Calabrese et al., 2014; Inoue and Tsuda, 2018). We tested the role for microglia *Bdnf* in neuroplasticity 24 h post-MCAO. For this we assessed changes in synaptic markers (VGLUT1,GAD65/67, $GABA_AR$ γ2 and $GABA_AR$ α5) in both ipsi- and contra-lateral hemispheres compared to $BDNF^{Tg/Tg}$ / $CX3CR1^{CreERT2/+}$ control animals at 24 h post-MCAO and observed no significant changes in the double transgene mice (Suppl. Fig. 6a-d). We also performed WB analysis to measure α1 and α2 $GABA_AR$ subunit expression level change in the double transgene mice after MCAO (Suppl. Fig 2g, h). Our analysis confirmed that synaptic receptors expression is unchanged upon *Bdnf* gene depletion from microglia cells. We used $BDNF^{wt/wt}$ / $CX3CR1^{CreERT2/+}$ and $BDNF^{Tg/Tg}$ / $CX3CR1^{CreERT2/+}$ mice to culture microglia from post-natal day 3 pups and infected them with AAV-Cre virus to confirm *Bdnf* gene deletion in microglia cells. qRT-PCR analysis confirmed significant reduction in *Bdnf* mRNA specifically from $BDNF^{Tg/Tg}$ / $CX3CR1^{CreERT2/+}$ mice

(Suppl. Fig. 6e). Our results uncover a consistent pattern of synapse preservation and tissue preservation at 24 h post-MCAO in both *Gphn*S268A/S270A mutant mice and BDNF$^{Tg/Tg}$ / CX3CR1$^{CreERT2/+}$ double transgene mouse line, suggesting that gephyrin phosphorylation downstream of BDNF perhaps activates a feedback signal for microglia activation.

The density of astrocytes is reduced in BDNF$^{Tg/Tg}$ / CX3CR1Cre$^{+/-}$ double transgene mouse line in comparison to WT (Suppl. Fig. 4a'). However, this does not give us a clear indication of neuroinflammation and glia activation in BDNF$^{Tg/Tg}$ / CX3CR1Cre$^{+/-}$ double transgene mouse line at 24 h post-MCAO. To assess inflammation, we stained for IBA-1 and CD11b in BDNF$^{Tg/Tg}$ / CX3CR1Cre$^{+/-}$ sham and MCAO animals and could observe no changes in both hemispheres (Suppl. Fig. 6f, g, g', h). Interestingly, we could observe normalization of microglia hyperthrophy in the ipsi-lateral side (Suppl. Fig. 6g). When we measured for GFAP process length, we found significant hypertrophy in both the hemispheres 24 h after MCAO (Suppl. Fig. 6h, i), perhaps obtaining hyper vigilance state due to reduced cell number. These results support our idea that prevention of microglia BDNF release after ischemia reduce brain inflammation.

As a control, we also assessed neuroinflammation in BDNF$^{wt/wt}$ / CX3CR1Cre$^{+/-}$ mouse line at 24 h post-MCAO. We stained for IBA-1 and CD11b and could observe significant shortening of microglial process length in the ipsi-lateral and a significant increase in the contra lateral hemisphere similar as in WT mice (Suppl. Fig. 6j-k'). GFAP staining also showed retracted processes in the ipsi-lateral hemisphere and extended process length in the contra-lateral hemisphere (Suppl. Fig. 6 l, m).

Bdnf deletion from microglia or GphnS268A/S270A mutation prevent BDNF increase

If a gephyrin scaffold stability contributes towards microglia activation after MCAO, then it should be reflected in proBDNF and mBDNF level changes in our different mouse lines. We assessed for changes in proBDNF and mBDNF using WB assay in both ipsi- and contra-lateral hemispheres at 24 h after MCAO. First, we compared the baseline levels of proBDNF and mBDNF across WT, WT mice treated with PLX5622, *Gphn*S268A/S270A mutant mice, $BDNF^{wt/wt}$ / $CX3CR1Cre^{+/-}$ and $BDNF^{Tg/Tg}$ / $CX3CR1Cre^{+/-}$ mice. In comparison to WT mice, WT mice treated with PLX5622 showed elevated levels of proBDNF and $BDNF^{Tg/Tg}$ / $CX3CR1Cre^{+/-}$ mice exhibited significantly lower levels of proBDNF, while others had levels similar to WT control (Suppl. Fig. 7a, a'). The analysis of mBDNF across different mice lines showed no significant differences from WT (Suppl. Fig. 7a'').

Once we established the baseline differences in proBDNF and mBDNF expression across mice lines used in our study, we went on to compare intra-mouse changes in proBDNF and mBDNF in both the hemispheres 24 h post-MCAO. In WT mice, we observed a significant increase in both pro- and mature- forms of BDNF specifically in the ipsi-lateral side; there was a small increase in the contra-lateral side but it was not significant (Suppl. Fig. 7b-b''). We next assessed for BDNF level changes in the *Gphn*S268A/S270A mutant mice, quantification of the WB showed that proBDNF levels show a significant reduction in the contra-lateral hemisphere compared to the ipsi-lateral side (Suppl. Fig. 7c-c'). However, mBDNF expression levels remained unchanged in both hemispheres (Suppl. Fig. 7c''). In WT mice treated with PLX5622, we saw a significant reduction of pro-BDNF level in both the hemispheres (Suppl. Fig. 7d-d'). However, mBDNF levels showed no changes within both ipsi- and contra-lateral hemispheres (Suppl. Fig. 7d''). Testing $BDNF^{Tg/Tg}$ / $CX3CR1^{CreERT2/+}$ double transgene mice for proBDNF

and mBDNF level changes at 24 h post ischemia showed no significant difference in proBDNF levels in both hemispheres. On the other hand, mBDNF levels were significantly reduced in both ipsi- and contra-lateral hemispheres (Suppl. Fig. 7e-e''). These observations suggests that microglia is an important source of proBDNF and mBDNF after MCAO. Furthermore, our data links gephyrin phosphorylation at S268 and S270 for proBDNF and mBDNF release from microglia following MCAO.

If indeed mBDNF increase after MCAO is the main determinant for gephyrin protein stability and phosphorylation at Ser 268, Ser 270, then WT mice treated with PLX5622 or $BDNF^{Tg/Tg}$ / $CX3CR1^{CreERT2+/-}$ mice should stabilize gephyrin protein along with reduction in Ser268 and Ser270 phosphorylation. To confirm this, we performed WB analysis for changes in gephyrin protein and phosphorylation levels. We observed stabilization of gephyrin protein in both PLX5622 treated and $BDNF^{Tg/Tg}$ / $CX3CR1^{CreERT2/+}$ mice at 24 h post MCAO (Suppl. Fig 3h, i, l, m). In addition, we observed reduced gephyrin phosphorylation at S268 and S270 sites in both PLX5622 treated and $BDNF^{Tg/Tg}$;$CX3CR1^{CreERT2/+}$ mice (Suppl. Fig. 3j, k, n , o). These results further confirm that mBDNF from microglia after MCAO initiate gephyrin phosphorylation and synapse loss following cerebral ischemia.

Discussion:

This study reveals a direct connection between microglia, BDNF signaling and gephyrin phosphorylation as a key pathway regulating tissue integrity and synapse loss after ischemic stroke. Preventing BDNF release from microglia or preventing gephyrin phosphorylation at Ser 268 and Ser 270 are equally protective against ischemic injury. Specifically, we demonstrate that (a) proBDNF and mBDNF act through $p75^{NTR}$ and TrkB receptors respectively to facilitate

glutamatergic and GABAergic synapse loss after ischemia; (b) ERK1/2 and GSK3β kinase phosphorylate gephyrin at Ser 268 and Ser 270 downstream of TrkB for GABAergic synapse downregulation; (c) *in vivo* pharmacological depletion of microglia or microglia-specific *Bdnf* gene deletion or expression of gephyrin phospho-null S268A/S270A mutant, protect against ischemic brain injury and synapse loss at 24 h post-MCAO; (d) GphnS268A/S270A mutant mice block neuroinflammation and synapse loss at 24 h post-MCAO. Taken together, microglia activation, proBDNF and mBDNF secretion are tightly coupled to glutamatergic and GABAergic synapse integrity in a model of ischemia-induced brain injury.

GABAergic system in ischemia

Our results concur with previous observations in the gerbil wherein following transient cerebral ischemia (24 h) $GABA_A$Rs are downregulated (Alicke and Schwartz-Bloom, 2002). In mice, it was reported that tonic GABA currents are increased in the penumbra 3 days after ischemia. An impairment in GABA transporter GAT3/GAT4 function was shown to contribute towards upregulation of extrasynaptic α5 and δ $GABA_A$R tonic current (Clarkson et al., 2010). In this study, we report reduction in synaptic $GABA_A$R subunits α1, α2, γ2 and also extrasynaptic α5 subunit expression at 24 h after ischemia (Fig. 2; Suppl. Fig. 2). In addition, we report that presynaptic GAD65/67 terminals are also significantly reduced at 24 h after ischemia. Importantly, our data indicates that by stabilizing GABAergic synaptic and extrasynaptic transmission, one can reduce ischemic brain damage (Fig. 7a, b). It has also been reported that inverse agonists specific for α5-subunit-containing extrasynaptic $GABA_A$ receptors administered 4 days after stroke promotes early stroke recover (Clarkson et al., 2010). Hence, it is conceivable that increase in extrasynaptic $GABA_A$Rs observed at 4 day post ischemia is a homeostatic

response to the early reduction in GABA and $GABA_A$Rs. This could explain the neuroprotection observed in *Gphn*268A/S270A mutant mice at 24 h post ischemia.

Postsynaptic scaffold stability after ischemia

In WT mice, 24 h post MCAO gephyrin protein levels are reduced (Suppl. Fig. 3e); however, we observe no change in PSD95 clusters, as a proxy for glutamatergic synapses (Fig. 5c). After ischemia nNOS interaction with PSD95 has been reported to stabilize the protein at postsynaptic sites (Zhou et al., 2010). In GphnS268A/S270A mutant mice, PSD95 clusters are unaffected in the ipsi- and contra-lateral hemispheres (Fig. 6b'). Gephyrin has also been reported to interact with nNOS (Dejanovic and Schwarz, 2014). It remains to be tested whether interaction with nNOS is influenced by ERK1/2 and GSK3β phosphorylation of gephyrin. Reduced gephyrin expression after MCAO might make nNOS available for PSD95 interaction. If neuroinflammation is the trigger for nNOS activation, our data shows reduced inflammation in *Gphn*S268A/S270A mutant mice and $BDNF^{Tg/Tg}$; $CX3CR1^{CreERT2/+}$ double transgene mice. Therefore, BDNF signaling could increase neuroinflammation by activating nNOS after ischemia.

proBDNF and mBDNF signaling regulate synaptic functions

At the neuromuscular junction, proBDNF and mBDNF elicit opposite effects by promoting axon retraction through activation of $p75^{NTR}$ on presynaptic site or potentiate synapse through TrkB activation at the postsynaptic site respectively. Neuronal activity converts proBDNF to mBDNF, serving as a reward signal to stabilize synaptic contacts and strengthen neurotransmission (Je et al., 2013) However, within hippocampal neurons, proBDNF has been reported to activate $p75^{NTR}$

localized in dendritic spines of CA1 neurons and enhance NR2B-dependent LTD (Woo et al., 2005).

In the current study, we present evidence for proBDNF and mBDNF in glutamatergic and GABAergic synapse down regulation after ischemia. $p75^{NTR}$ lack intrinsic enzymatic activity and activate signal transduction pathway by associating with adaptor proteins that are distinct from TrkB signaling cascade (Kaplan and Miller, 2000). Consistent with this literature, our data shows the specificity for proBDNF and $p75^{NTR}$ signaling for spine downregulation and mBDNF and TrkB for gephyrin regulation at GABAergic postsynaptic sites (Fig.3). Our study has important implications. First, we uncover synapse plasticity function for proBDNF and $p75^{NTR}$ in ischemic brain, which is in marked contrast to its role in regulating neuronal apoptosis. Second, our results show that TrkB and downstream pathways (ERK1/2 and GSK3β) specifically influence shaft synapse and not spine synapse stability (Fig.4). Third, our data suggests that endogenous ratio of proBDNF and mBDNF is influenced by microglia, rather than neuron or astrocyte (Suppl. Fig. 7).

Microglia as a source of BDNF in ischemia

Deletion of BDNF from specific subpopulation of neurons has revealed that both presynaptic and postsynaptic BDNF contributes to specific aspects of LTP. For example, presynaptic BDNF was documented to increase the strength of LTP, while postsynaptic BDNF facilitates LTP maintenance (Lin et al., 2018). In addition, BDNF release from dendritic spines can activate NMDA and TrkB receptors within the same release site to influence structural plasticity (Hedrick et al., 2016). At GABAergic terminals, time duration of exogenous BDNF exposure has opposite effects on $GABA_AR$ and gephyrin clustering. In hippocampal neuron culture, short-term

(5 min) BDNF application inhibits $GABA_AR$ internalization through phosphoinositide-3 kinase (PI-3 kinase) and PKC pathways (Jovanovic et al., 2004). However, long-term (90 min) BDNF application reduces $GABA_AR$ and gephyrin clustering (Brünig et al., 2001). Presynaptically, BDNF regulates GAD65 mRNA expression through the recruitment of ERK pathway, leading to cAMP-response element (CRE)-binding protein (CREB) activation (Sánchez-Huertas and Rico, 2010).

To add to this complexity, BDNF is not only found in neurons but also expressed in both astrocytes and microglia (Ferrini and Koninck, 2013; Parkhurst et al., 2013). Within the spinal cord circuit, BDNF activates TrkB in lamina I neurons to downregulate KCC2 (Chloride potassium symporter), thereby increasing intracellular chloride concentration and reversing GABAergic inhibition to cause neuronal depolarization (Inoue and Tsuda, 2018). The resulting hyperexcitability of neurons contributes to mechanical hypersensitivity. Microglia-specific *Bdnf* knockout reduces PNI-induced pain (Sorge et al., 2015). In the current study, we report microglia as the major source of BDNF after ischemia for glutamatergic and GABAergic synapse regulation. The release of BDNF from microglia has been linked to purinergic receptor P2X4R activation, causing disinhibition of pain-transmitting spinal lamina I neurons (Beggs et al., 2012; Masuda et al., 2014). The expression of P2X4R increases after exposure to proinflammatory cytokines such as INF-γ (Tsuda et al., 2009). Microglia can sense extracellular ATP through P2Y12R to migrate (Ohsawa et al., 2007), or P2X7R to be activated (Monif et al., 2009). Hence, it is possible that within 24 h post ischemia inflammation activates P2X4R expression to promote BDNF protein synthesis and release.

Gephyrin phosphorylation influences microglia activation

During acute ischemic stroke natural killer (NK) cells infiltrate periinfarct areas of the brain to promote inflammation (e.g. microglia activation) and neuronal damage. Interestingly, depletion of NK cells within the first 12 h after MCAO attenuates neurological deficits and infarct volume (Gan et al., 2014). Here, we report that microglia depletion using PLX5622 (Suppl. Fig 5) and *Bdnf* gene deletion specifically from microglia (Suppl. Fig. 6) prevent glutamatergic and GABAergic synapse loss and reduce the extent of infarct volume (Fig. 7a, b) after ischemia. Hence, it is possible that NK cells influence infarct development through microglia activation and local BDNF release to trigger glutamatergic and GABAergic synapse loss. Furthermore, in addition to activation of microglia, we uncover activation of ERK1/2 and GSK3β pathways (Suppl. Fig. 3b, c) 24 h post ischemia. As a direct target of ERK1/2 (Tyagarajan et al., 2013)and GSK3β (Tyagarajan et al., 2011), gephyrin phosphorylation at Ser268 and Ser270 sites are significantly increased after ischemia, while total gephyrin level is decreased (Suppl. Fig. 3 e-g). Stabilization of gephyrin clusters through the expression of S268A/S270A mutant in hippocampal slice culture selectively prevents GABAergic synapse loss after ischemia (Fig. 4h, i). In *Gphn*S268A/S270A mutant mice both glutamatergic and GABAergic synapse loss can be prevented (Fig. 6). This suggests to us that mechanisms activated after ischemia *in vivo* might be similar to mechanisms operational in organotypic slice cultures after OGD.

We reveal a link between gephyrin phosphorylation at Ser268 and Ser270, microglia activation and BDNF secretion (see model; Fig. 8). In this model, (1) mBDNF signaling after MCAO would trigger gephyrin phosphorylation at SerS268 and Ser270; (2) stabilization of mBDNF increase after MCAO in *Gphn*268A/S270A mutant mice suggests that gephyrin scaffold stability controls microglia activation; (3) microglia activation would trigger glutamatergic spine synapse collapse through $p75^{NTR}$ signaling and downstream RhoA/Rac activation for actin

regulation; (4) retracted spines could facilitate microglia aided stripping of VGLUT terminals. On the other hand, (5) sustained TrkB activation would ensure gephyrin phosphorylation at Ser268 and Ser270; (6) gephyrin scaffold loss would increase $GABA_AR$ internalization and microglia aided GAD65/67 terminal stripping. It has been reported that microglia physically displace GABAergic presynaptic terminals after lipopolysaccharide (LPS) induced inflammation (Chen et al., 2014). Together, our data shows that silencing neurotransmission at the initial 24 h post-MCAO facilitates tissue protection and synapse recovery in the penumbra.

Experimental Procedures:

Ethics Statement

All animal handling procedures were carried out consistent with guidelines set by the Canadian Council on Animal Care, the European Community Council Directives of November 24, 1986 (86/609/EEC) and approved by the cantonal veterinary office of Zurich (ZH219/15). All procedures were approved by the Animal Resource Committee of the School of Medicine at McGill University and are outlined in McGill University Animal Handling Protocol #5057.

Hippocampal Slice Cultures and Oxygen-Glucose Deprivation (OGD)

We have chosen to study the hippocampus as it possesses a unique unidirectional network that is preserved within organotypic cultures (Guérineau et al., 1997), making it an ideal candidate to study microcircuitry remodeling. Organotypic hippocampal slices were prepared using the roller-tube method, as previously described (Guérineau et al., 1997) with transgenic mice expressing membrane-targeted MARCKS-enhanced GFP under the Thy-1 promoter in a

subpopulation of CA1 cells (Paola et al., 2003). We used an established model of OGD as a model of ischemia (Gee et al., 2006), briefly, mature organotypic hippocampal slices were placed in a glass dish containing glucose-free Tyrode's solution (in mM: NaCl, 137; KCl, 2.7; $CaCl_2$, 2.5; $MgCl_2$, 2; $NaHCO_3$, 11.6; NaH_2PO_4, 0.4; pH 7.4) containing: 2 mM 2-Deoxyglucose, 3 mM sodium azide and 8 mM sucrose, for 4-5 minutes, and were then returned to culture media for 90 minutes, 24 hours or 1 week. Control slices were exposed to Tyrode's solution (in mM: NaCl, 137; KCl, 2.7; $CaCl_2$, 2.5; $MgCl_2$, 2; $NaHCO_3$, 11.6; NaH_2PO_4, 0.4; glucose, 5.6; pH 7.4) for 4-5 minutes and returned to culture media.

Mouse lines

*Gphn*S268A/S270A mutant mouse was generated using CRISPR/cas9 (Cyagen, USA) in BL6 background. B6.129P2(C)-Cx3cr1tm2.1(cre/ERT2) (Stock 020940) (Yona et al., 2012)mice and Bdnftm3Jae or $BDNF^{Tg}$ (Stock 004339) (Rios et al., 2001) were obtained from Jackson Laboratory to generate $BDNF^{Tg/Tg}$ / $CX3CR1^{ERT2Cre+/-}$ double transgene. The mice were injected (i.p) on four consequtive days with tamoxifen dissolved in corn oil (Sigma H-6278; 1mg/ day) to induce Cre expression at 4 weeks followed by sham or MCAO surgery at 8-9 weeks of age. Animals were random assigned and both genders were used for both conditions.

Middle cerebral artery occlusion (MCOA) model

Wild type C57Bl6/J-Crl1 mice were purchased from Charles River Laboratories (Germany), the *Gphn*S268A/S270A mutant, $BDNF^{Tg/Tg}$ / $CX3CR1^{ERT2Cre+/-}$ were bred in house. At 4 weeks age animals were randomly allocated to groups. The transient occlusion of the middle cerebral artery was conducted using the filament model as described previously (Vaas et al., 2017). Briefly,

anaesthesia was induced using 3% isoflurane in an oxygen/air (1:4) mixture and maintained at 2% Isoflurane. The area around the neck was shaved, disinfected and an incision was made along the midline. The common and the external carotid artery were isolated and ligated. A silicon rubber filament (Doccol, USA, Lot 701956RE) was inserted into the internal carotid artery to block the middle cerebral artery. The filament remained in place for 30min before reperfusion was allowed by withdrawing it. During occlusion the mouse was placed in a preheated (30°C) recovery box and allowed to recover from anaesthesia. After reperfusion, the internal carotid artery was ligated to prevent bleeding and the wound was sutured. Sham operation involved identical surgical procedures, but the filament was immediately withdrawn after insertion. A total volume of 500µl of Buprenorphine (0.03mg/g) with Saline was injected after surgery and consecutive after 4h and 8h s.c. The mouse was kept for 2h in the recovery box and then placed back into its home cage. Mashed food and food pellets were placed on the cage bottom to encourage food uptake.

Cresyl violet staining

To verify the success of the MCAO a cresyl violet staining was performed 24h after of reperfusion and infarct volume was assessed as percentage of the affected hemisphere. Five 20µm thick coronal sections taken at Bregma +2.8, +1.54, +0.14, −1.94 and −4.6mm, were stained with cresyl violet using vendor protocol and later digitalised using a Zeiss Axio Scan.Z1 at 5x magnification and lesions were determined using Zen Software (Zeiss). The person analysing was blinded to the treatment groups. Cerebral lesion volume was calculated summing up the volume of each section, while corrected for oedema (group numbers >4).

Immunofluorescence and Confocal Microscopy

Hippocampal organotypic slices

90 minutes after OGD induction, hippocampal slices were fixed for 1 hour at room temperature in 4% paraformaldehyde in 0.1 M phosphate buffer (PB), pH 7.4. Slices were then washed 5× in 0.1 M PB, permeabilized in 0.4% Triton X-100 and blocked with 1.5% heat inactivated horse serum overnight at 4°C. 1:500 anti-Gephyrin (Synaptic Systems) was incubated for 5 days at 4°C in permeabilizing buffer and washed 5× with 0.1 M PB containing 1.5% heat inactivated horse serum. Slices were incubated for 3 hours at room temperature with 1:250 anti-mouse DyLight 650 (Jackson ImmunoResearch, Burlington, ON, Canada) secondary antibody diluted in 0.1 M PB containing 1.5% heat inactivated horse serum. Following 5× washes with 0.1 M PB containing 1.5% heat-inactivated horse serum, slices were mounted with fluorescent mounting medium (DAKO, Mississauga, ON, Canada) onto microscope slides.

Slices were imaged using a Leica TCS SP2 scan head (Leica Microsystems) on a Leica DM6000 B upright microscope, equipped with HCX PL APO 63× NA 1.4 oil immersion objective using a 543 nm HeNe laser line. Image stacks were collected at Z = 0.3 μm and averaged 2-3 times to improve signal-to-noise ratio. For quantification, image stacks were obtained with identical parameters (laser intensity, filters, pinhole size, photomultiplier tube gain and offset). Representative images are maximum intensity projections of 5 sections from each stack.

In vivo slice imaging

24 hours following MCAO, P60-70 (male or female) mice were anesthetized by intraperitoneal pentobarbital injection (Nembutal; 50 mg/kg) and perfused transcardially with ice-cold

oxygenated ACSF (Notter et al., 2014), pH 7.4, for 2min. Brains were immediately fixed in 4% PFA for 3 hours at 4°C. After rinsing in PBS, brains were incubated in 30% sucrose (in PBS) at 4°C over-night. 45µm-thick coronal sections were cut from frozen blocks using a sliding microtome (HM400; Microm) and stored at -20°C in antifreeze solution. After 3 times 10 min washes in Tris-Triton Solution (50mM Tris, 150mM NaCl, 0.05% Trito X-100, pH 7.4), sections were incubated in primary antibody solution (50mM Tris, 150mM NaCl, 0.4% Triton X-100, 2% normal goat serum, pH 7.4) at 4°C overnight. Primary antibodies are listed in Table 1. Sections were washed 3 x 10min in Tris-Triton Solution and incubated in secondary antibody solution (50mM Tris, 150mM NaCl, 0.05% Triton X-100, 2% normal goat serum, pH 7.4) for 1 hour at room temperature with secondary antibodies raised in goat. All secondary antibodies used were diluted 1:500. Antibodies conjugated to AlexaFluor-488 and AlexaFluor-647 were purchased from Invitrogen, while antibodies conjugated to Cy3 were purchased from Jackson ImmunoResearch Laboratories. Sections were washed 3 times 10 min in Tris-Triton Solution and mounted on gelatin-coated slides using Fluorescence Mounting Medium (Dako). Z-stack images (4 optical sections, 0.75µm step size) were recorded of all sections using confocal laser scanning microscopy (LSM 700, Carl Zeiss). Images were taken using a 40x objective with a numerical aperture of 1.4, and pixel size of 112 nm^2. Three juxtaposed images of the motor cortex layer 2/3 were taken on the ipsi- and contra-lateral hemispheres. To reduce variability, multiple images were captured from 3 sections per mouse and total of 4-5 mice were analyzed per condition/genotype. Cluster density values were averaged from these sections. All imaging parameters were kept constant between MCAO and sham animals. For cluster analysis, a custom Python-script using the ImageJ image-processing framework was used. The script can be used as a plugin and is openly available on a github repository (https://github.com/dcolam/Cluster-

Analysis-Plugin). Representative example images were processed using ImageJ. Statistical tests were performed using Prism software (GraphPad) using 5 mice per group.

Dendrite Reconstructions, Spine Quantification, cluster Quantification

3D confocal stacks were deconvolved with Huygens Essentials software (Scientific Volume Imaging, Hilversum, The Netherlands) using a full maximum likelihood extrapolation algorithm. Stacks were then imported and rendered using the Surpass function in Imaris software (Bitplane AG). Experimenter was blinded to conditions and treatment groups, spines were manually counted and using the ratio of the diameter and length of the head and neck of spines it was possible to distinguish between stubby, mushroom, and thin subtypes of dendritic spines. These classifications were based on previously established criteria (McKinney, 2009). Lastly, *n* values for spine analysis represent ~75-100 µm of dendrite from 1-2 cells imaged from each slice. The number and volume of gephyrin clusters were quantified using the Spot function of Imaris software, which differentiates puncta based on the fluorescence intensity.

Electrophysiological Recordings and Analysis

Slices were transferred into a temperature-controlled chamber (25°C) mounted on an upright microscope (DM LFSA, Leica Microsystems) and continuously perfused with external solution. Patch recording electrodes were pulled from borosilicate glass (GC150TC; Clark Instruments, Old Sarum, Salisbury UK). All electrophysiological recordings were made using an Axopatch 200A amplifier (Molecular Devices, Sunnyvale, CA, U.S.A.).

AMPA-mediated mEPSCs were gathered from whole-cell voltage-clamp recordings of CA1 pyramidal neurons obtained at 25°C using electrodes with resistances of 4-5 MΩ and filled

with intracellular solution containing (in mM): K-Gluconate, 120; EGTA, 1; HEPES, 10; Mg-ATP, 5; Na-GTP 0.5; NaCl, 5; KCl, 5; phosphocreatine, 10; 295 mOsm; pH adjusted with KOH to 7.3. mEPSCs were recorded at -60 mV and in the presence of 1 µM tetrodotoxin (TTX), 15 µM 3-[(R)-2-carboxypiperazin-4-yl]-propyl-1-phosphonic acid (CPP), 100 µM picrotoxin, and 1 µM CGP55845 in the external Tyrode's solution. Access resistance was monitored with brief test pulses at regular intervals (2-3 minutes) throughout the experiment. Access resistance was usually 10-13 MΩ and data were discarded if the resistance deviated more than 10% through the course of the experiment. Series resistance of the access pulse and decay time was also used for the calculation of total membrane capacitance. After the holding current had stabilized, data were recorded at a sampling frequency of 10 kHz and filtered at 2 kHz for 10 to 15 minutes.

$GABA_AR$-mediated mIPSCs were gathered from whole-cell voltage-clamp recordings of CA1 pyramidal neurons obtained at 25°C using electrodes with resistances of 4-5 MΩ and filled with intracellular solution containing (in mM): CsCl, 140; NaCl, 4; 0.5, CaCl2; HEPES, 10; EGTA, 5; QX-314, 2; Mg-ATP, 2; Na-GTP 0.5; 290 mOsm; pH adjusted with CsOH to 7.36. mIPSCs were recorded at -60 mV and in the presence of 1 µM TTX, 25 µM CPP, 5 µM CGP55845, 5 µm 6-cyano-7-nitroquinoxaline-2,3-dione (CNQX) and 0.3 µm strychnine in external Tyrode's solution. Access resistance was monitored with brief test pulses at regular intervals (2-3 minutes) throughout the experiment. After the holding current had stabilized, data were recorded at a sampling frequency of 10 kHz and filtered at 2 kHz for 10 to 15 minutes.

All mEPSCs and mIPSCs were detected offline using the Mini Analysis Software (Synaptosoft, Decatur, GA, USA). The amplitude threshold for mEPSC and mIPSCs detection was set at four times the root-mean-square value of a visually event-free recording period. From every experiment, 5 minutes of stable recording was randomly selected for blinded analysis of

amplitude and inter-event interval. The data obtained was then used to plot cumulative histograms with an equal contribution from every cell. For statistical analysis, data were averaged for every single cell. It should be noted that the amplitude analysis was conducted only on single mEPSCs and mIPSCs that did not have subsequent events occurring during their rising and decaying phases. For frequency analysis, all selected events were considered.

Pharmacological Treatments

To scavenge BDNF, slices were treated with TrkB-Fc (R&D Systems; Minneapolis, MN, USA), a fusion protein in which the BDNF binding site of the TrkB receptor replaces the Fc fragment of a human IgG1 antibody. We found that TrkB-Fc treatment to hippocampal cultures for 24 hours downregulated TrkB receptor phosphorylation (data not shown). TrkB-Fc was diluted in culture media at a final concentration of 10 µg/ml and treatment began immediately following induction of OGD. ERK activation was inhibited using 30 µM of MEK inhibitor PD98059 (Tocris Biosciences, ON, Burlington, Canada), GSK3β activity was inhibited using 25 µM GSK3β-IX (Tocris Biosciences). PD98059 and GSK3β-IX were diluted in dimethyl sulfoxide (Invitrogen) and treatment began overnight prior to OGD induction, removed during induction and continued for 90 minutes after. Control sister cultures were treated with control culture media containing dimethyl sulfoxide only. The following function blocking antibodies were used: 1:200 anti-$p75^{NTR}$ (kind gift from Dr. P. Barker, McGill University, Montreal, QC, Canada; Rex antibody for more information see (Weskamp and Reichardt, 1991), 1:200 anti-proBDNF (kind gift from Dr. Philip Barker, McGill University, Montreal, Canada) and 1:100 anti-mBDNF (N-9, Developmental Studies Hybridoma Bank, University of Iowa, IA, USA; for more information

see (Kolbeck et al., 2008). Function blocking antibody treatment began 2 hours prior to OGD induction, removed during induction and continued for 90 minutes after.

Biolistic Gene Transfection

Cartridges were prepared according to manufacturer's protocol (Bio-Rad, Helios Gene Gun). Briefly, 15 mg of gold particles (1 μm diameter) were first coated with 0.05 M spermidine. 15 μg of plasmid DNA expressing tdTomato and 45 μg of wildtype gephyrin-GFP ($gephyrin_{WT}$-GFP) or dephosphorylation mutant gephyrin-GFP S268A/S270A ($gephyrin_{S268A/S270A}$-GFP). Plasmids were then precipitated onto the particles by adding CaCl2. The coated particles were resuspended into 100% ethanol and infused into Tefzel tubing, which were then coated with the particles. Coated tubing was cut into 0.5 inch cartridges which were then transfected into mature organotypic slice cultures by shooting at a distance of 2 cm with a pressure of 200 psi through a nylon mesh. Following 48 hours, slices which expressed target plasmids in CA1 pyramidal neurons were processed with OGD or control Tyrode solution.

Western blotting

24 hours following MCAO, mice were killed by decapitation and brains were dissected on ice. The ipsi- and contralateral cortices were immediately transferred to lysis buffer (50 mM Tris, pH 7.6, 150 mM NaCl, 1% Triton X-100, CompleteMini Protease Inhibitor Mixture, Roche). The cortices were homogenized and incubated on ice for 1 hour. Lysates were centrifuged at 20,000 RPM for 30 min at 4°C, and supernatants were stored at -80°C. Samples were run on Tris-glycine polyacrylamide gels and proteins were transferred to PVDF membranes. Primary antibodies (see Table 1) were incubated in Tris-buffered saline with 0.05% Tween 20 (TBST),

including 5% WesternBlocking Solution (Roche) overnight at 4°C. Membranes were washed 5 x 5min in TBST. HRP-coupled donkey secondary antibodies (1:30,000) and fluorescent-coupled donkey secondary antibodies (1:20,000) were incubated for 30 min at room temperature, and membranes were washed again 5 times 5 min in TBST. Fluorescent signals were captured using the Odyssey® CLx Imager. SuperSignal West Pico ChemiluminescentSubstrate (Thermo Fisher Scientific) was applied to visualize HRP labelled antibodies and developed using the FUJIFILM Luminescent Image Analyzer LAS-1000 plus & Intelligent Dark Box II (Fujifilm). Images were analyzed using ImageJ and statistical tests were performed using Prism software (GraphPad) using a minimum of 4 mice per group.

Statistical Analysis

For the slice culture comparisons we performed 2-way ANOVA and independent t-tests on the following figures: Figure 2b,d,e, ,f',f,g,g'; Figure 3b,c,d,f,g,h; Figure 4b,c,d,g,h,I. The t-tests were performed to confirm significance between conditions as 2-way ANOVA and post hoc test does not cover all the comparisons of our interest. These t-test p values are unprotected, therefore we adjusted them using Bonferroni correction (e.g. if the set of the data is compared 5 times, we need to multiply the p-value by 5). The listed significant comparisons all have protected p-values by Bonferroni post-test. *** $p<0.001$; **$p<0.01$; *$p<0.05$.

Comparison between two groups were made using two-tailed independent Student's *t*-test. Comparisons between multiple groups and treatments were made using two-way ANOVA with *post hoc* Bonferroni multiple comparison test. Comparisons between multiple groups were made using one-way ANOVA. Cumulative probability plots were compared using Kolmogorov-Smirnov test for probability distributions. Results are expressed as mean ± S.E.M.

Author Contributions

SKT and RAM designed the study. ZST and PKYC performed and analyzed the OGD electrophysiology. RG performed and analysed the morphology data from OGD experiments. ZST, PKYC and RG supported data collection and analysis. MV performed the MCAO, TC, MV and SS performed and analysed the mouse MCAO data. SBN performed data analysis. RCP, PAB and JK provided technical expertise, infrastructure support and biological reagents for this study. RG, PKYC, ZST prepared OGD figures, TC, SS, SBN, MV and SKT prepared MCAO figures. All authors contributed to writing and editing the manuscript.

Acknowledgments:

We thank Dr. J-M. Fritschy for antibody reagents and feedback on the manuscript; F. Charron for preparation and maintenance of cultures; G.Bosshard for preparation of microglia cultures; Plexxikon for sharing their PLX5622 chow formulated compound for our studies. This project was initiated as part of ZNZ-McGill-Oxford tripartite collaboration. This work was supported by grants from CIHR to RAM (grant ID: MOP 133611), Savoy Foundation to RAM, Swiss National Science Foundation (320030_179277), ERA-NET NEURON (32NE30_173678/1), the Synapsis Foundation and the Vontobel foundation to JK, Swiss National Science Foundation grant to SKT (31003A_159867), internal UZH funding to SKT, Forschungskredit Candoc grant to TC and Forschungskredit postdoc grant to MV.

Competing financial interests

The authors declare no competing financial interests.

References

Adachi, N., Numakawa, T., Richards, M., Nakajima, S., and Kunugi, H. (2014). New insight in expression, transport, and secretion of brain-derived neurotrophic factor: Implications in brain-related diseases. World J Biological Chem *5*, 409–428.

Albers, G.W., Goldstein, L.B., Hall, D., Lesko, L.M., and Investigators, for the A.A.S. (2001). Aptiganel Hydrochloride in Acute Ischemic Stroke. Jama *286*, 2673.

Alicke, B., and Schwartz-Bloom, R.D. (2002). Rapid Down-Regulation of GABAA Receptors in the Gerbil Hippocampus Following Transient Cerebral Ischemia. J Neurochem *65*, 2808–2811.

Beggs, S., Trang, T., and Salter, M.W. (2012). P2X4R+ microglia drive neuropathic pain. Nat Neurosci *15*, 1068–1073.

Béjot, Y., Prigent-Tessier, A., Cachia, C., Giroud, M., Mossiat, C., Bertrand, N., Garnier, P., and Marie, C. (2010). Time-dependent contribution of non neuronal cells to BDNF production after ischemic stroke in rats. Neurochem Int *58*, 102–111.

Bergeron, M., Yu, A.Y., Solway, K.E., Semenza, G.L., and Sharp, F.R. (1999). Induction of hypoxia-inducible factor-1 (HIF-1) and its target genes following focal ischaemia in rat brain. Eur J Neurosci *11*, 4159–4170.

Brouns, R., and Deyn, P.P.D. (2009). The complexity of neurobiological processes in acute ischemic stroke. Clin Neurol Neurosur *111*, 483–495.

Brünig, I., Penschuck, S., Berninger, B., Benson, J.A., and Fritschy, J.M. (2001). BDNF reduces miniature inhibitory postsynaptic currents by rapid downregulation of GABAA receptor surface expression. European Journal of Neuroscience *13*, 1320–1328.

Buscemi, L., Price, M., Bezzi, P., and Hirt, L. (2019). Spatio-temporal overview of neuroinflammation in an experimental mouse stroke model. Sci Rep-Uk *9*, 507.

Calabrese, F., Rossetti, A.C., Racagni, G., Gass, P., Riva, M.A., and Molteni, R. (2014). Brain-derived neurotrophic factor: a bridge between inflammation and neuroplasticity. Front Cell Neurosci *8*, 430.

Campbell, B.C.V., Silva, D.A.D., Macleod, M.R., Coutts, S.B., Schwamm, L.H., Davis, S.M., and Donnan, G.A. (2019). Ischaemic stroke. Nat Rev Dis Primers *5*, 70.

Chen, Z., Jalabi, W., Shpargel, K.B., Farabaugh, K.T., Dutta, R., Yin, X., Kidd, G.J., Bergmann, C.C., Stohlman, S.A., and Trapp, B.D. (2012). Lipopolysaccharide-induced microglial activation and neuroprotection against experimental brain injury is independent of hematogenous TLR4. J Neurosci Official J Soc Neurosci *32*, 11706–11715.

Chen, Z., Jalabi, W., Hu, W., Park, H.-J., Gale, J.T., Kidd, G.J., Bernatowicz, R., Gossman, Z.C., Chen, J.T., Dutta, R., et al. (2014). Microglial displacement of inhibitory synapses provides neuroprotection in the adult brain. Nat Commun *5*, 4486.

Clarkson, A.N., Huang, B.S., Macisaac, S.E., Mody, I., and Carmichael, S.T. (2010). Reducing excessive GABA-mediated tonic inhibition promotes functional recovery after stroke. Nature *468*, 305–309.

Cserép, C., Pósfai, B., Lénárt, N., Fekete, R., László, Z.I., Lele, Z., Orsolits, B., Molnár, G., Heindl, S., Schwarcz, A.D., et al. (2019). Microglia monitor and protect neuronal function through specialized somatic purinergic junctions. Sci New York N Y *367*, 528–537.

Dejanovic, B., and Schwarz, G. (2014). Neuronal nitric oxide synthase-dependent S-nitrosylation of gephyrin regulates gephyrin clustering at GABAergic synapses. The Journal of Neuroscience : The Official Journal of the Society for Neuroscience *34*, 7763–7768.

Elmore, M.R.P., Najafi, A.R., Koike, M.A., Dagher, N.N., Spangenberg, E.E., Rice, R.A., Kitazawa, M., Matusow, B., Nguyen, H., West, B.L., et al. (2014). Colony-stimulating factor 1 receptor signaling is necessary for microglia viability, unmasking a microglia progenitor cell in the adult brain. Neuron *82*, 380–397.

Elmore, M.R.P., Hohsfield, L.A., Kramár, E.A., Soreq, L., Lee, R.J., Pham, S.T., Najafi, A.R., Spangenberg, E.E., Wood, M.A., West, B.L., et al. (2018). Replacement of microglia in the aged brain reverses cognitive, synaptic, and neuronal deficits in mice. Aging Cell *17*, e12832.

Ferrini, F., and Koninck, Y.D. (2013). Microglia control neuronal network excitability via BDNF signalling. Neural Plast *2013*, 429815.

Fumagalli, S., Perego, C., Ortolano, F., and Simoni, M.-G.D. (2013). CX3CR1 deficiency induces an early protective inflammatory environment in ischemic mice. Glia *61*, 827–842.

Gan, Y., Liu, Q., Wu, W., Yin, J.-X., Bai, X.-F., Shen, R., Wang, Y., Chen, J., Cava, A.L., Poursine-Laurent, J., et al. (2014). Ischemic neurons recruit natural killer cells that accelerate brain infarction. P Natl Acad Sci Usa *111*, 2704–2709.

Gee, C.E., Benquet, P., Raineteau, O., Rietschin, L., Kirbach, S.W., and Gerber, U. (2006). NMDA receptors and the differential ischemic vulnerability of hippocampal neurons. European Journal of Neuroscience *23*, 2595–2603.

Gibson, L.M., Brazzelli, M., Thomas, B.M., and Sandercock, P.A.G. (2010). A systematic review of clinical trials of pharmacological interventions for acute ischaemic stroke (1955-2008) that were completed, but not published in full. Trials *11*, 43.

Gill, R., Chang, P.K.-Y., Prenosil, G.A., Deane, E.C., and McKinney, R.A. (2013). Blocking brain-derived neurotrophic factor inhibits injury-induced hyperexcitability of hippocampal CA3 neurons. Eur J Neurosci *38*, 3554–3566.

Gomes, C., Ferreira, R., George, J., Sanches, R., Rodrigues, D.I., Gonçalves, N., and Cunha, R.A. (2013). Activation of microglial cells triggers a release of brain-derived neurotrophic factor (BDNF) inducing their proliferation in an adenosine A2A receptor-dependent manner: A2A receptor blockade prevents BDNF release and proliferation of microglia. J Neuroinflamm *10*, 16.

Gottlieb, M., Bonova, P., Danielisova, V., Nemethova, M., Burda, J., and Cizkova, D. (2013). Brain-derived neurotrophic factor blood levels in two models of transient brain ischemia in rats. Gen Physiol Biophys *32*, 139–142.

Guérineau, N.C., McKinney, R.A., Debanne, D., Mollard, P., and Gähwiler, B.H. (1997). Organotypic cultures of the rat anterior pituitary: morphology, physiology and cell-to-cell communication. J Neurosci Meth *73*, 169–176.

Hedrick, N.G., Harward, S.C., Hall, C.E., Murakoshi, H., McNamara, J.O., and Yasuda, R. (2016). Rho GTPase complementation underlies BDNF-dependent homo- and heterosynaptic plasticity. Nature *538*, 104–108.

Inoue, K., and Tsuda, M. (2018). Microglia in neuropathic pain: cellular and molecular mechanisms and therapeutic potential. Nat Rev Neurosci *19*, 138–152.

Jang, S.-W., Liu, X., Yepes, M., Shepherd, K.R., Miller, G.W., Liu, Y., Wilson, W.D., Xiao, G., Blanchi, B., Sun, Y.E., et al. (2010). A selective TrkB agonist with potent neurotrophic activities by 7,8-dihydroxyflavone. P Natl Acad Sci Usa *107*, 2687–2692.

Je, H.S., Yang, F., Ji, Y., Potluri, S., Fu, X.-Q., Luo, Z.-G., Nagappan, G., Chan, J.P., Hempstead, B., Son, Y.-J., et al. (2013). ProBDNF and mature BDNF as punishment and reward signals for synapse elimination at mouse neuromuscular junctions. J Neurosci Official J Soc Neurosci *33*, 9957–9962.

Jiang, Y., Wei, N., Zhu, J., Lu, T., Chen, Z., Xu, G., and Liu, X. (2010). Effects of brain-derived neurotrophic factor on local inflammation in experimental stroke of rat. Mediat Inflamm *2010*, 372423.

Kaplan, D.R., and Miller, F.D. (2000). Neurotrophin signal transduction in the nervous system. Curr Opin Neurobiol *10*, 381–391.

Kolbeck, R., Bartke, I., Eberle, W., and Barde, Y.-A. (2008). Brain-Derived Neurotrophic Factor Levels in the Nervous System of Wild-Type and Neurotrophin Gene Mutant Mice. J Neurochem *72*, 1930–1938.

Kraemer, B.R., Yoon, S.O., and Carter, B.D. (2014). Handb Exp Pharmacol *220*, 121–164.

Lai, S.-W., Chen, J.-H., Lin, H.-Y., Liu, Y.-S., Tsai, C.-F., Chang, P.-C., Lu, D.-Y., and Lin, C. (2018). Regulatory Effects of Neuroinflammatory Responses Through Brain-Derived Neurotrophic Factor Signaling in Microglial Cells. Mol Neurobiol *55*, 7487–7499.

Lakhan, S.E., Kirchgessner, A., and Hofer, M. (2009). Inflammatory mechanisms in ischemic stroke: therapeutic approaches. J Transl Med *7*, 97.

Lenz, K.M., and Nelson, L.H. (2018). Microglia and Beyond: Innate Immune Cells As Regulators of Brain Development and Behavioral Function. Front Immunol *9*, 698.

Lenz, K.M., Nugent, B.M., Haliyur, R., and McCarthy, M.M. (2013). Microglia are essential to masculinization of brain and behavior. The Journal of Neuroscience : The Official Journal of the Society for Neuroscience *33*, 2761–2772.

Li, Y., Du, X.-F., Liu, C.-S., Wen, Z.-L., and Du, J.-L. (2012). Reciprocal regulation between resting microglial dynamics and neuronal activity in vivo. Dev Cell *23*, 1189–1202.

Lin, P.-Y., Kavalali, E.T., and Monteggia, L.M. (2018). Genetic Dissection of Presynaptic and Postsynaptic BDNF-TrkB Signaling in Synaptic Efficacy of CA3-CA1 Synapses. Cell Reports *24*, 1550–1561.

Lyden, P.D., Jackson-Friedman, C., Shin, C., and Hassid, S. (2000). Synergistic Combinatorial Stroke Therapy: A Quantal Bioassay of a GABA Agonist and a Glutamate Antagonist. Exp Neurol *163*, 477–489.

Masuda, T., Iwamoto, S., Yoshinaga, R., Tozaki-Saitoh, H., Nishiyama, A., Mak, T.W., Tamura, T., Tsuda, M., and Inoue, K. (2014). Transcription factor IRF5 drives P2X4R+-reactive microglia gating neuropathic pain. Nat Commun *5*, 3771.

McKinney, R.A. (2009). Excitatory amino acid involvement in dendritic spine formation, maintenance and remodelling. J Physiology *588*, 107–116.

Monif, M., Reid, C.A., Powell, K.L., Smart, M.L., and Williams, D.A. (2009). The P2X7 Receptor Drives Microglial Activation and Proliferation: A Trophic Role for P2X7R Pore. J Neurosci *29*, 3781–3791.

Morris, G.P., Wright, A.L., Tan, R.P., Gladbach, A., Ittner, L.M., and Vissel, B. (2016). A Comparative Study of Variables Influencing Ischemic Injury in the Longa and Koizumi Methods of Intraluminal Filament Middle Cerebral Artery Occlusion in Mice. Plos One *11*, e0148503.

Mou, L., Dias, B.G., Gosnell, H., and Ressler, K.J. (2013). Gephyrin plays a key role in BDNF-dependent regulation of amygdala surface GABAARs. Neuroscience *255*, 33–44.

Notter, T., Panzanelli, P., Pfister, S., Mircsof, D., and Fritschy, J.-M. (2014). A protocol for concurrent high-quality immunohistochemical and biochemical analyses in adult mouse central nervous system. The European Journal of Neuroscience *39*, 165–175.

Ohsawa, K., Irino, Y., Nakamura, Y., Akazawa, C., Inoue, K., and Kohsaka, S. (2007). Involvement of P2X 4 and P2Y 12 receptors in ATP-induced microglial chemotaxis. Glia *55*, 604–616.

Paola, V.D., Arber, S., and Caroni, P. (2003). AMPA receptors regulate dynamic equilibrium of presynaptic terminals in mature hippocampal networks. Nat Neurosci *6*, 491–500.

Paolicelli, R.C., Jawaid, A., Henstridge, C.M., Valeri, A., Merlini, M., Robinson, J.L., Lee, E.B., Rose, J., Appel, S., Lee, V.M.-Y., et al. (2017). TDP-43 Depletion in Microglia Promotes Amyloid Clearance but Also Induces Synapse Loss. Neuron *95*, 297-308.e6.

Parkhurst, C.N., Yang, G., Ninan, I., Savas, J.N., Yates, J.R., Lafaille, J.J., Hempstead, B.L., Littman, D.R., and Gan, W.-B. (2013). Microglia promote learning-dependent synapse formation through brain-derived neurotrophic factor. Cell *155*, 1596–1609.

Rajan, W.D., Wojtas, B., Gielniewski, B., Gieryng, A., Zawadzka, M., and Kaminska, B. (2018). Dissecting functional phenotypes of microglia and macrophages in the rat brain after transient cerebral ischemia. Glia *67*, 232–245.

Reemst, K., Noctor, S.C., Lucassen, P.J., and Hol, E.M. (2016). The Indispensable Roles of Microglia and Astrocytes during Brain Development. Front Hum Neurosci *10*, 566.

Rios, M., Fan, G., Fekete, C., Kelly, J., Bates, B., Kuehn, R., Lechan, R.M., and Jaenisch, R. (2001). Conditional Deletion Of Brain-Derived Neurotrophic Factor in the Postnatal Brain Leads to Obesity and Hyperactivity. Mol Endocrinol *15*, 1748–1757.

Sánchez-Huertas, C., and Rico, B. (2010). CREB-Dependent Regulation of GAD65 Transcription by BDNF/TrkB in Cortical Interneurons. Cereb Cortex New York N Y 1991 *21*, 777–788.

Scha□bitz, W.-R., Steigleder, T., Cooper-Kuhn, C.M., Schwab, S., Sommer, C., Schneider, A., and Kuhn, H.G. (2007). Intravenous Brain-Derived Neurotrophic Factor Enhances Poststroke Sensorimotor Recovery and Stimulates Neurogenesis. Stroke *38*, 2165–2172.

Schafer, D.P., and Stevens, B. (2015). Microglia Function in Central Nervous System Development and Plasticity. Csh Perspect Biol *7*, a020545.

Shuaib, A., Lees, K.R., Lyden, P., Grotta, J., Davalos, A., Davis, S.M., Diener, H.-C., Ashwood, T., Wasiewski, W.W., Emeribe, U., et al. (2007). NXY-059 for the Treatment of Acute Ischemic Stroke. New Engl J Med *357*, 562–571.

Sorge, R.E., Mapplebeck, J.C.S., Rosen, S., Beggs, S., Taves, S., Alexander, J.K., Martin, L.J., Austin, J.-S., Sotocinal, S.G., Chen, D., et al. (2015). Different immune cells mediate mechanical pain hypersensitivity in male and female mice. Nat Neurosci *18*, 1081–1083.

Spangenberg, E.E., Lee, R.J., Najafi, A.R., Rice, R.A., Elmore, M.R.P., Blurton-Jones, M., West, B.L., and Green, K.N. (2016). Eliminating microglia in Alzheimer's mice prevents neuronal loss without modulating amyloid-β pathology. Brain J Neurology *139*, 1265–1281.

Tanaka, J.-I., Horiike, Y., Matsuzaki, M., Miyazaki, T., Ellis-Davies, G.C.R., and Kasai, H. (2008). Protein synthesis and neurotrophin-dependent structural plasticity of single dendritic spines. Sci New York N Y *319*, 1683–1687.

Tsuda, M., Masuda, T., Kitano, J., Shimoyama, H., Tozaki-Saitoh, H., and Inoue, K. (2009). IFN-gamma receptor signaling mediates spinal microglia activation driving neuropathic pain. P Natl Acad Sci Usa *106*, 8032–8037.

Tyagarajan, S.K., Ghosh, H., Yévenes, G.E., Nikonenko, I., Ebeling, C., Schwerdel, C., Sidler, C., Zeilhofer, H.U., Gerrits, B., Muller, D., et al. (2011). Regulation of GABAergic synapse formation and plasticity by GSK3beta-dependent phosphorylation of gephyrin. Proceedings of the National Academy of Sciences *108*, 379–384.

Tyagarajan, S.K., Ghosh, H., Yévenes, G.E., Imanishi, S.Y., Zeilhofer, H.U., Gerrits, B., and Fritschy, J.-M. (2013). Extracellular signal-regulated kinase and glycogen synthase kinase 3β regulate gephyrin postsynaptic aggregation and GABAergic synaptic function in a calpain-dependent mechanism. The Journal of Biological Chemistry *288*, 9634–9647.

Vaas, M., Ni, R., Rudin, M., Kipar, A., and Klohs, J. (2017). Extracerebral Tissue Damage in the Intraluminal Filament Mouse Model of Middle Cerebral Artery Occlusion. Front Neurol *8*, 85.

Wei, Z., Chigurupati, S., Arumugam, T.V., Jo, D.-G., Li, H., and Chan, S.L. (2011). Notch Activation Enhances the Microglia-Mediated Inflammatory Response Associated With Focal Cerebral Ischemia. Stroke *42*, 2589–2594.

Weskamp, G., and Reichardt, L.F. (1991). Evidence that biological activity of NGF is mediated through a novel subclass of high affinity receptors. Neuron *6*, 649–663.

Woo, N.H., Teng, H.K., Siao, C.-J., Chiaruttini, C., Pang, P.T., Milner, T.A., Hempstead, B.L., and Lu, B. (2005). Activation of p75NTR by proBDNF facilitates hippocampal long-term depression. Nat Neurosci *8*, 1069–1077.

Wood, H. (2019). A role for double-negative T cells in post-stroke neuroinflammation. Nat Rev Neurol *15*, 246–247.

Yang, J., Harte-Hargrove, L.C., Siao, C.-J., Marinic, T., Clarke, R., Ma, Q., Jing, D., Lafrancois, J.J., Bath, K.G., Mark, W., et al. (2014). proBDNF negatively regulates neuronal remodeling, synaptic transmission, and synaptic plasticity in hippocampus. Cell Reports *7*, 796–806.

Yassi, N., Churilov, L., Campbell, B.C.V., Sharma, G., Bammer, R., Desmond, P.M., Parsons, M.W., Albers, G.W., Donnan, G.A., Davis, S.M., et al. (2015). The Association between Lesion Location and Functional Outcome after Ischemic Stroke. Int J Stroke *10*, 1270–1276.

Yona, S., Kim, K.-W., Wolf, Y., Mildner, A., Varol, D., Breker, M., Strauss-Ayali, D., Viukov, S., Guilliams, M., Misharin, A., et al. (2012). Fate mapping reveals origins and dynamics of monocytes and tissue macrophages under homeostasis. Immunity *38*, 79–91.

Yu, S.-J., Tseng, K.-Y., Shen, H., Harvey, B.K., Airavaara, M., and Wang, Y. (2013). Local administration of AAV-BDNF to subventricular zone induces functional recovery in stroke rats. Plos One *8*, e81750.

Zhang, J., Liu, J., Li, D., Zhang, C., and Liu, M. (2019). Calcium antagonists for acute ischemic stroke. Cochrane Database Syst Rev *2*, CD001928.

Zhang, S., Boyd, J., Delaney, K., and Murphy, T.H. (2005). Rapid Reversible Changes in Dendritic Spine Structure In Vivo Gated by the Degree of Ischemia. J Neurosci *25*, 5333–5338.

Zhou, L., Li, F., Xu, H.-B., Luo, C.-X., Wu, H.-Y., Zhu, M.-M., Lu, W., Ji, X., Zhou, Q.-G., and Zhu, D.-Y. (2010). Treatment of cerebral ischemia by disrupting ischemia-induced interaction of nNOS with PSD-95. Nat Med *16*, 1439–1443.

Figure Legends:

Figure 1 – OGD induces morphological and functional deficits in excitatory synapses.

(a) Example tertiary dendrites from CA1 pyramidal neurons expressing myristoylated-eGFP in control versus 90 min post-OGD organotypic hippocampal cultures. Scale = 2 µm. **(b)** Quantification of dendritic spines categorized into stubby, mushroom and long thin subtypes (*p < 0.05 and **p < 0.01, two-tailed independent Student's t-test). Total spine density (spines/µm of dendrite): Control – 1.76 ± 0.08 (n = 8); OGD – 1.25 ± 0.11 (n = 8). **(c)** Example images of maximum intensity projections of area CA1 immunostained for gephyrin and VGAT in control cultures versus 90 min following OGD. **(d)** Quantification of number of gephyrin clusters per confocal stack (consisting of five 512x512 pixel z-planes each; ***p < 0.0001, two-tailed independent Student's t-test; gephyrin cluster values were normalized to control). Mean number (A.U.): Control – 1.00 ± 0.03 (n = 10 slices); OGD – 0.40 ± 0.05 (n = 10 slices). **(e)** Quantification of the total volume of gephyrin cluster (***p < 0.0001, two-tailed independent Student's t-test). Mean volume (A.U.): Control – 1.00 ± 0.05; OGD – 0.53 ± 0.03. **(f)** Cumulative probability histogram of mean amplitude (p < 0.001, Kolmogorov-Smirnov test). **(f')** Cumulative probability histogram for IEIs of mEPSCs (p < 0.05, Kolmogorov-Smirnov test). **(g)** Cumulative probability histogram of mean amplitude of mIPSCs (p < 0.001, Kolmogorov-Smirnov test). **(g')** Cumulative probability histogram for IEIs of mIPSCs (p < 0.05, Kolmogorov-Smirnov test).

Figure 2 – Scavenging BDNF rescues OGD-induced synapse deficits

(a) Example dendrites from CA1 neurons expressing myristoylated-eGFP with and without TrkB-fc treatment. Scale = 2 µm. **(b)** Quantification of dendritic spines (*p < 0.05, Two-way

ANOVA with Bonferroni multiple comparison test). Total spine density (spines/µm of dendrite): Control – 1.22 ± 0.05 (*n* = 16); Control+TrkB-Fc – 1.40 ± 0.10 (*n* = 12); OGD – 0.95 ± 0.06 (*n* = 12); OGD+TrkB-Fc – 1.19 ± 0.07 (*n* = 14). **(c)** Example images of maximum intensity projections of organotypic hippocampal slices immunostained for gephyrin with and without TrkB-Fc treatment. Scale = 2 µm. **(d)** Quantification of number of gephyrin puncta per confocal stack (consisting of five 512x512 pixel z-planes each; ***$p < 0.0001$, Two-way ANOVA with Bonferroni multiple comparison test; all gephyrin values were normalized to control). Mean number (A.U.): Control – 1.00 ± 0.04 (*n* = 15); Control+TrkB-Fc – 0.95 ± 0.04 (*n* = 9 slices); OGD – 0.27 ± 0.03 (*n* = 13); OGD+TrkB-Fc – 0.86 ± 0.05 (*n* = 13). **(e)** Quantification of gephyrin puncta volume (***$p < 0.0001$, Two-way ANOVA with Bonferroni multiple comparison test). Mean volume (A.U.): Control – 1.00 ± 0.03; Control+TrkB-Fc – 0.98 ± 0.03; OGD – 0.67 ± 0.06; OGD+TrkB-Fc – 1.02 ± 0.04. **(f)** Cumulative probability histogram of mean amplitude ($p < 0.001$, Two-way ANOVA with Bonferroni multiple comparison test). **(f')** Cumulative probability histogram for IEIs of mEPSCs ($p < 0.05$, Two-way ANOVA with Bonferroni multiple comparison test). **(g)** Cumulative probability histogram of mean amplitude of mIPSCs ($p > 0.05$, Two-way ANOVA with Bonferroni multiple comparison test). **(g')** Cumulative probability histogram for IEIs of mIPSCs ($p < 0.05$, Two-way ANOVA with Bonferroni multiple comparison test).

Figure 3 – Differential proBDNF and mBDNF signaling induce synapse loss after ischemia. **(a)** Example tertiary dendrites from CA1 pyramidal neurons of organotypic hippocampal slices immunostained for gephyrin, with or without anti-proBDNF or anti-$p75^{NTR}$ (Rex) treatment before OGD. Scale = 2 µm. **(b)** Dendritic spine quantification (***$p < 0.0001$ Two-way

ANOVA with Bonferroni multiple comparison test). Total spine density (spines/µm of dendrite): Control – 1.43 ± 0.04 (*n* = 15); Control+anti-proBDNF – 1.37 ± 0.07 (*n* = 15); Control+anti-p75^{NTR} – 1.42 ± 0.05 (*n* = 15); OGD – 0.95 ± 0.04 (*n* = 39); OGD+anti-proBDNF – 1.40 ± 0.03 (*n* = 30); OGD+anti-p75^{NTR} – 1.35 ± 0.04 (*n* = 32). **(c)** Quantification of number of gephyrin cluster density (consisting of five 512x512 pixel z-planes each; ***$p < 0.0001$, Two-way ANOVA with Bonferroni multiple comparison test, compared to control and treated controls; all gephyrin values were normalized to control). Mean number (A.U.): Control – 1.00 ± 0.03 (*n* = 18 slices); Control+anti-proBDNF – 0.97 ± 0.07 (*n* = 6); Control+anti-p75^{NTR} – 0.97 ± 0.06 (*n* = 6); OGD – 0.43 ± 0.03 (*n* = 20 slices); OGD+anti-proBDNF – 0.47 ± 0.03 (*n* = 16 slices); OGD+anti-p75^{NTR} – 0.47 ± 0.04 (*n* = 9). **(d)** Quantification of gephyrin puncta volume (***$p < 0.0001$, Two-way ANOVA with Bonferroni multiple comparison test, compared to control and treated controls). Mean volume (A.U.): Control – 1.00 ± 0.04; Control+anti-proBDNF – 0.95 ± 0.07; Control+anti-p75^{NTR} – 1.01 ± 0.09; OGD – 0.63 ± 0.03; OGD+anti-proBDNF – 0.65 ± 0.02; OGD+anti-p75^{NTR} – 0.62 ± 0.03. **(e)** Example tertiary dendrites from CA1 pyramidal neurons of organotypic hippocampal slices immunostained for gephyrin, with or without anti-mBDNF (N-9) treatment before OGD. Scale = 2 µm. **(f)** Quantification of dendritic spines (**$p < 0.001$ Two-way ANOVA with Bonferroni multiple comparison test). Total spine density (spines/µm of dendrite): Control – 1.45 ± 0.04 (*n* = 34); Control+anti-mBDNF (N-9) – 1.37 ± 0.03 (*n* = 17); OGD – 0.95 ± 0.05 (*n* = 31); OGD+anti-N-9 – 1.05 ± 0.06 (*n* = 19). **(g)** Quantification of number of gephyrin clusters per confocal stack; consisting of five 512x512 pixel z-planes each (***$p <$ 0.0001, Two-way ANOVA with Bonferroni multiple comparison test; all gephyrin values were normalized to control). Mean number (A.U.): Control – 1.00 ± 0.03 (*n* = 11); Control+N-9 – 0.99 ± 0.04 (*n* = 6 slices); OGD – 0.44 ± 0.04 (*n* = 12); OGD+ anti-mBDNF (N-9) – 0.85 ± 0.06 (*n* =

8). **(h)** Quantification of gephyrin cluster volume (***$p < 0.0001$, Two-way ANOVA with Bonferroni multiple comparison test). Mean volume (A.U.): Control – 1.00 ± 0.06; Control+N-9 – 1.07 ± 0.06; OGD – 0.66 ± 0.05; OGD+N-9 – 0.88 ± 0.05.

Figure 4 –ERK1/2 and GSK3β pathways induce gephyrin degradation but not dendritic spine loss after OGD.

(a) Example tertiary dendrites from CA1 pyramidal neurons from control and 90 minute post-OGD slices, immunostained for gephyrin, with or without pharmacological treatment (GSK3β inhibitor: GSK3β-IX and MEK inhibitor: PD98059). Scale = 2 µm. **(b)** Dendritic spine quantification (**$p < 0.01$ Two-way ANOVA with Bonferroni multiple comparison test). Total spine density (spines/µm of dendrite): Control – 1.41 ± 0.06 ($n = 21$); Control+PD+G.-IX – 1.46 ± 0.07 ($n = 19$); OGD – 1.09 ± 0.06 ($n = 22$); OGD+PD+G.-IX – 1.15 ± 0.05 ($n = 21$). **(c)** Quantification of number of gephyrin cluster density (consisting of five 512x512 pixel z-planes each; **$p < 0.001$, Two-way ANOVA with Bonferroni multiple comparison test; all gephyrin values were normalized to control). (d) Quantification of number of gephyrin cluster volume. Mean number (A.U.): Control – 1.00 ± 0.08 ($n = 11$); Control+PD+G.-IX – 1.12 ± 0.08 ($n = 9$); OGD – 0.44 ± 0.08 ($n = 9$); OGD+PD+G.-IX – 1.16 ± 0.09 ($n = 9$). **(d)** Quantification of gephyrin puncta volume (**$p < 0.001$, Two-way ANOVA with Bonferroni multiple comparison test). Mean volume (A.U.): Control – 1.00 ± 0.04; Control+PD+G.-IX – 0.91 ± 0.05; OGD – 0.67 ± 0.04; OGD+PD+G.-IX – 0.96 ± 0.07. **(e)** Maximum intensity projection of example CA1 pyramidal neurons which had been biolistitally transfected with a plasmid expressing tdTomato. Scale = 10 µm. Neurons were cotransfected with either wildtype or mutant gephyrin. **(f)** Example tertiary dendrites from CA1 pyramidal neurons from control and 90 minute post-OGD

slices which were transfected with either eGFP-gephyrin$_{WT}$ or eGFP-gephyrin$_{S268A/S270A}$. **(g)** Dendritic spine quantification (**p < 0.01 Two-way ANOVA with Bonferroni multiple comparison test). Total spine density (spines/μm of dendrite): Control + gephyrin$_{WT}$-GFP – 1.05 ± 0.052 (n = 11); Control + eGFP-gephyrin$_{S268A/S270A}$ – 1.05 ± 0.090 (n = 12); OGD – eGFP-gephyrin$_{WT}$ 0.74 ± 0.056 (n = 14); OGD + eGFP-gephyrin$_{S268A/S270A}$– 0.69 ± 0.064 (n = 8); **p < 0.01, Two-way ANOVA with Bonferroni multiple comparison test). **(h)** Quantification of number of gephyrin cluster density (**p < 0.01, Two-way ANOVA with Bonferroni multiple comparison test). Density: Control + eGFP-gephyrin$_{WT}$ – 0.38 ± 0.58; Control + eGFP-gephyrin$_{S268A/S270A}$ – 0.47 ± 0.092; OGD + eGFP-gephyrin$_{WT}$ – 0.11 ± 0.015; OGD+ eGFP-gephyrin$_{S268A/S270A}$– 0.44 ± 0.12. **(i)** Quantification of gephyrin cluster volume (**p < 0.01, Two-way ANOVA with Bonferroni multiple comparison test). Mean volume: Control + eGFP-gephyrin$_{WT}$ – 0. 85 ± 0.012; Control + eGFP-gephyrin$_{S268A/S270A}$ – 0.22 ± 0.043; OGD + eGFP-gephyrin$_{WT}$– 0.046 ± 0.01; OGD+ eGFP-gephyrin$_{S268A/S270A}$ – 0.21 ± 0.049.

Figure 5 - Synapse changes in the penumbra of ipsi-lateral hemispheres 24 h following MCAO.

(a) Example composite images for glutamatergic synaptic proteins (VGLUT1 and PSD95) and GABAergic synaptic markers (GAD65/67, γ2 and α5 GABA$_A$Rs). **(b)** Quantification for VGLUT1 cluster density (One-way ANOVA, Bonferroni multiple comparison post-hoc test; F(2,49)=11.2; P<0.0001). **(b')** Quantification for PSD95 cluster density (One-way ANOVA, Bonferroni multiple comparison post-hoc test; F(2,49)=0.84; P=0.43). **(c-d)** Quantification for GAD65/67 (One-way ANOVA, Bonferroni multiple comparison post-hoc test; F(2,10)=7.9; P=0.0085), γ2 (One-way ANOVA, Bonferroni multiple comparison post-hoc test; F(2,9)=6.4;

P=0.018) and α5 $GABA_AR$ cluster density (One-way ANOVA, Bonferroni multiple comparison test; F(2,9)=8.3; P=0.0088). Data shown as mean ± s.d. (N≥4); *P<0.05; **P<0.01; ***P<0.001. **(e)** qRT-PCR for *Bdnf* transcript in microglia culture derived from $BDNF^{wt/wt}$ / $CX3CR1^{ERT2Cre+/-}$ or $BDNF^{Tg/Tg}$ / $CX3CR1^{ERT2Cre+/-}$ and infected with AAV-Cre virus for 5 days (n=6); Students t-test.

Figure 6 – Synapse loss is attenuated in GphnS268A/S270A mutant mice 24 h following MCAO. **(a)** Example images of immunohistochemical stainings from motor cortex L2/3 ipsi- and contra-lateral sides in *Gphn*S268A/S270A mutant mice 24 h following MCAO. Glutamatergic synaptic terminals were visualised using VGLUT1 and PSD95 (shown as composite). GABAergic synaptic sites were visualised using GAD65/67, γ2 and α5 $GABA_ARs$. **(b)** Quantification for VGLUT1 (One-way ANOVA, Brown-Forsythe test; F(2,11)=o.35; P=0.70). **(b')** Quantification of PSD95 cluster density (One-way ANOVA, Brown-Forsythe test; F(2,11)=1.03; P=0.38). **(c)** Quantification for GAD65/67 (One-way ANOVA, Bonferroni multiple comparison test; F(2,9)=11.9; P=0.003). **(c')** Quantification of γ2 (One-way ANOVA, Bonferroni multiple comparison test; F(2,11)=0.60; P=0.56). **(c'')** Quantification of α5 $GABA_ARs$ clusters (One-way ANOVA, Bonferroni multiple comparison test; F(2,11)=4.9; P=0.02). Data shown as mean ± s.d. (N≥4).

Figure 7 – GphnS268A/S270A mutant mice show reduced neuroinflammation 24 h following MCAO. **(a)** Quantification of infarct volume in WT, $BDNF^{Tg/Tg}$ / $CX3CR1^{ERT2Cre+/-}$ double transgene mice or *Gphn*S268A/S270A mutant mice at 24 h following MCAO (One-way ANOVA, Brown-Forsythe test; F(2,15)=8.9; P=0.0028). **(b)** Example image of volumetry

analysis from 24 h post MCAO tissue sections from WT, $BDNF^{Tg/Tg}$ / $CX3CR1^{ERT2Cre+/-}$ double transgene mice and *Gphn*S268A/S270A mutant mice. Results expressed as mean ± s.d. (N=8). **(c)** Example images of WT mice stained 24 h following MCAO for microglia markers IBA1 and CD11b (shown as composite) and astrocyte marker GFAP. **(d)** Quantification for IBA1 process length in ipsi- and contra-lateral sides after MCAO . **(d')** Quantification for CD11b intensity in ipsi- and contra-lateral sides after MCAO. **(e)** Quantification for GFAP process length in ipsi- and contra-lateral sides after MCAO. **(f)** Zoom in image of IBA1 stained microglia showing reduced process length in the ipsi-lateral side 24 h post-MCAO in WT mice. **(g)** Example images of *Gphn*S268A/S270A mutant mice stained 24 h following MCAO for microglia markers IBA1 and CD11b (shown as composite) and astrocyte marker GFAP. **(h)** Quantification for IBA1 process length in ipsi- and contra-lateral sides after MCAO. **(h')** Quantification for CD11b intensity in ipsi- and contra-lateral sides after MCAO. **(i)** Quantification for GFAP process length in ipsi- and contra-lateral sides after MCAO. **(j)** Zoom in image of IBA1 stained microglia showing increased process length in the contra-lateral side 24 h post-MCAO in *Gphn*S268A/S270A mutant mice. Results expressed as mean ± s.d. (N=4); *P<0.05 (One-way ANOVA, Bonferroni multiple comparison test).

Figure 8 – Model for activated microlgia-mediated synapse removal at 24 h after ischemia. **(1)** post-MCAO ERK1/2 and GSK3β pathways downstream of mBDNF signaling phosphorylate gephyrin at S268 and S270 residues respectively, leading to gephyrin scaffold loss and protein degradation. **(2)** Gephyrin loss activates microglia to stimulate further release of proBDNF and mBDNF; **(3)** proBDNF acts on $p75^{NTR}$ to activate RhoA/Rac pathway for actin remodeling and spine loss. **(4)** spine loss triggers microglia aided stripping of VGLUT terminal; **(5)** mBDNF

release activate TrkB to sustain low levels of gephyrin protein; **(6)** reduced gephyrin facilitate $GABA_AR$ internalization and microglia aided displacement of GABAergic terminals. The dampening of excitatory and inhibitory neurotransmission provides neuroprotection for recovery after ischemia.

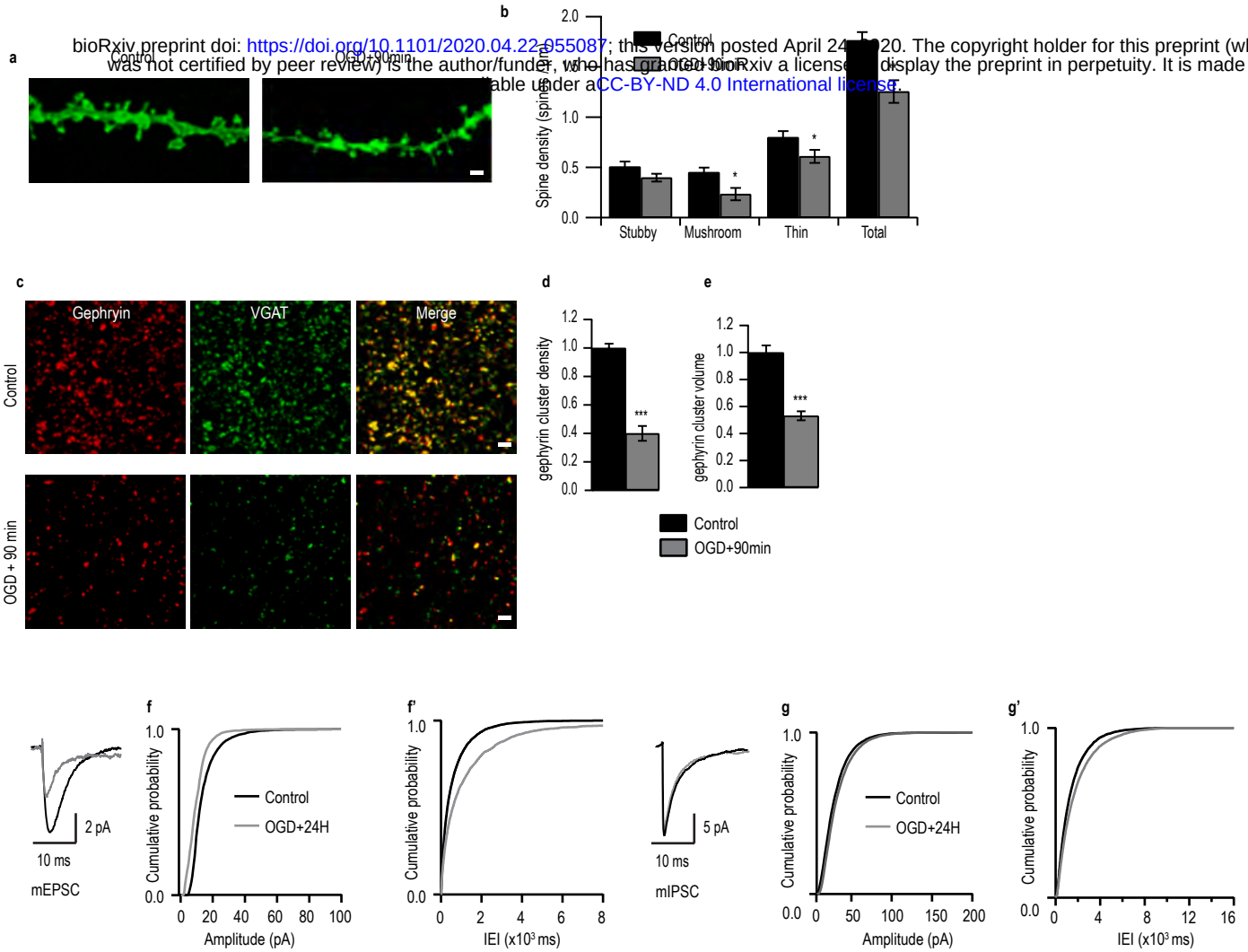

Cramer et al., Figure 1.

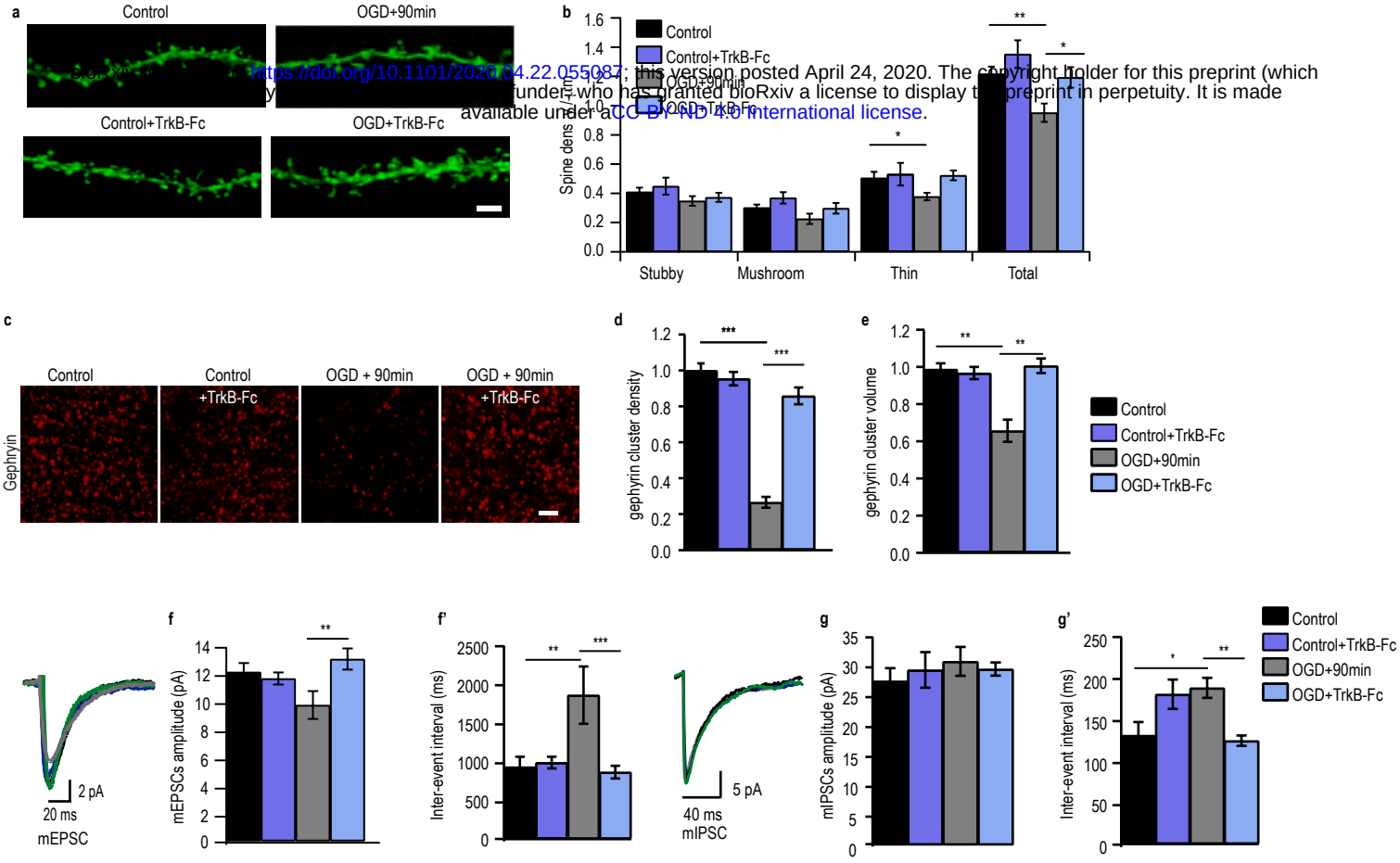

Cramer et al., Figure 2

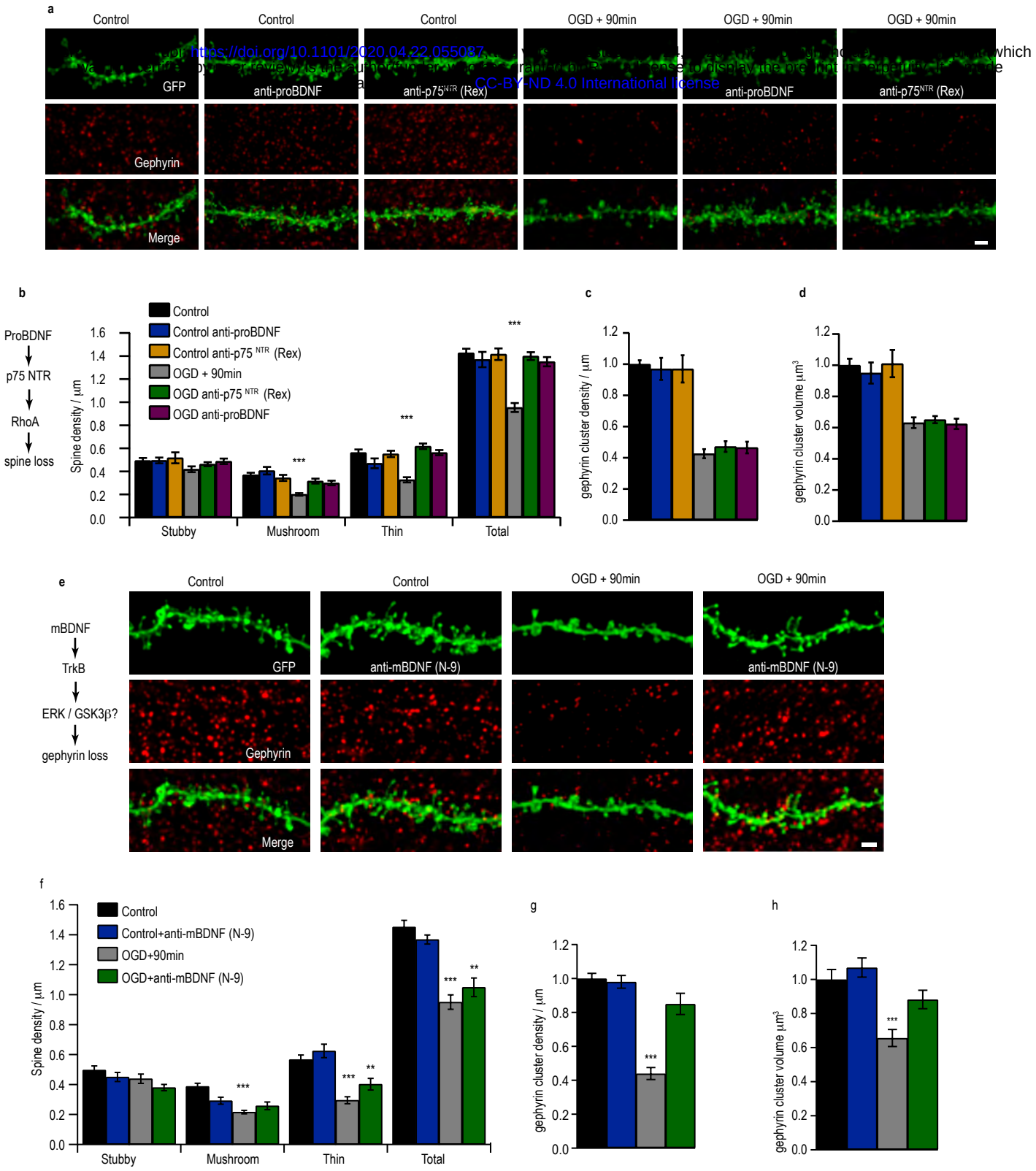

Cramer et al., Figure 3

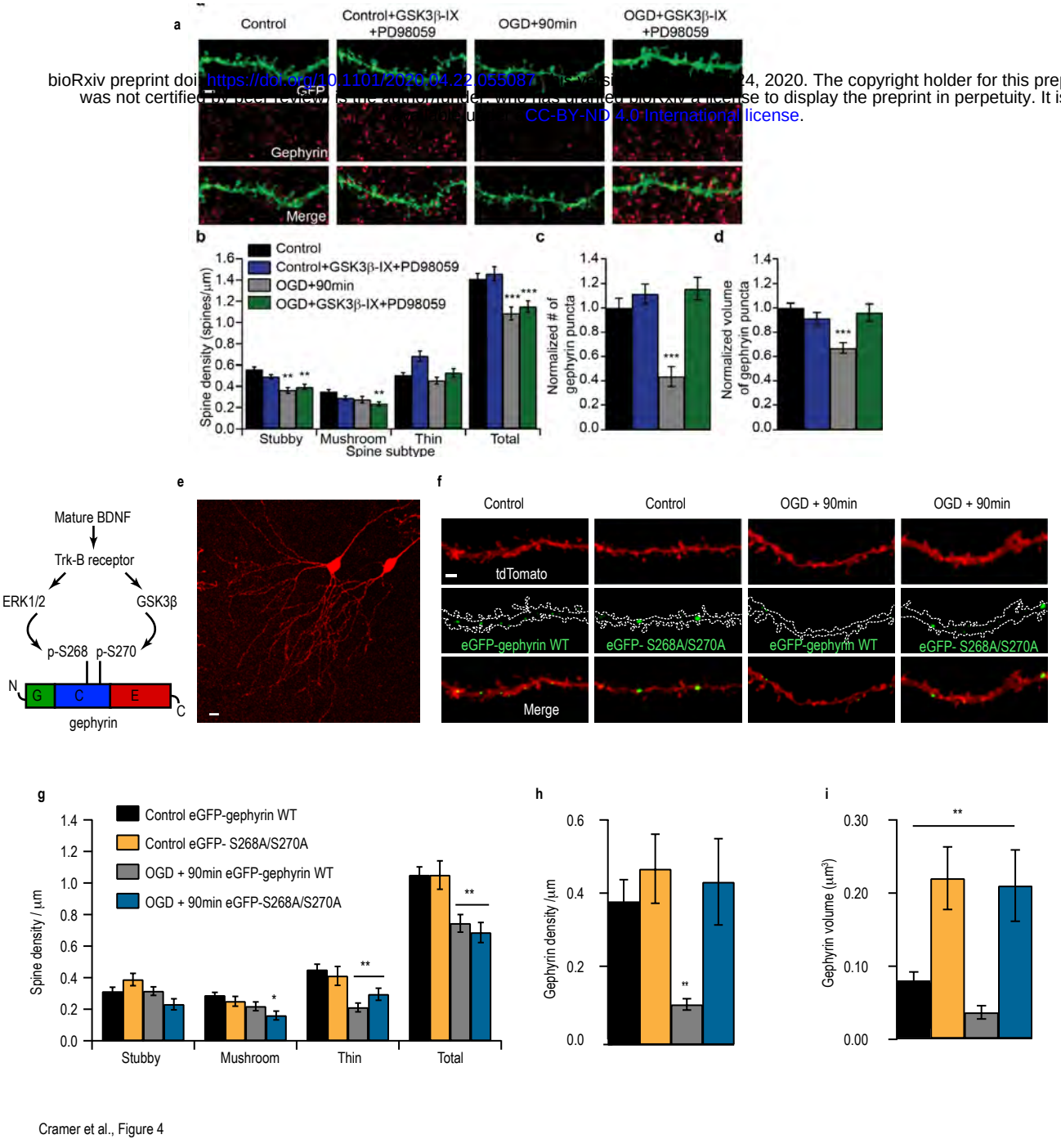

Cramer et al., Figure 4

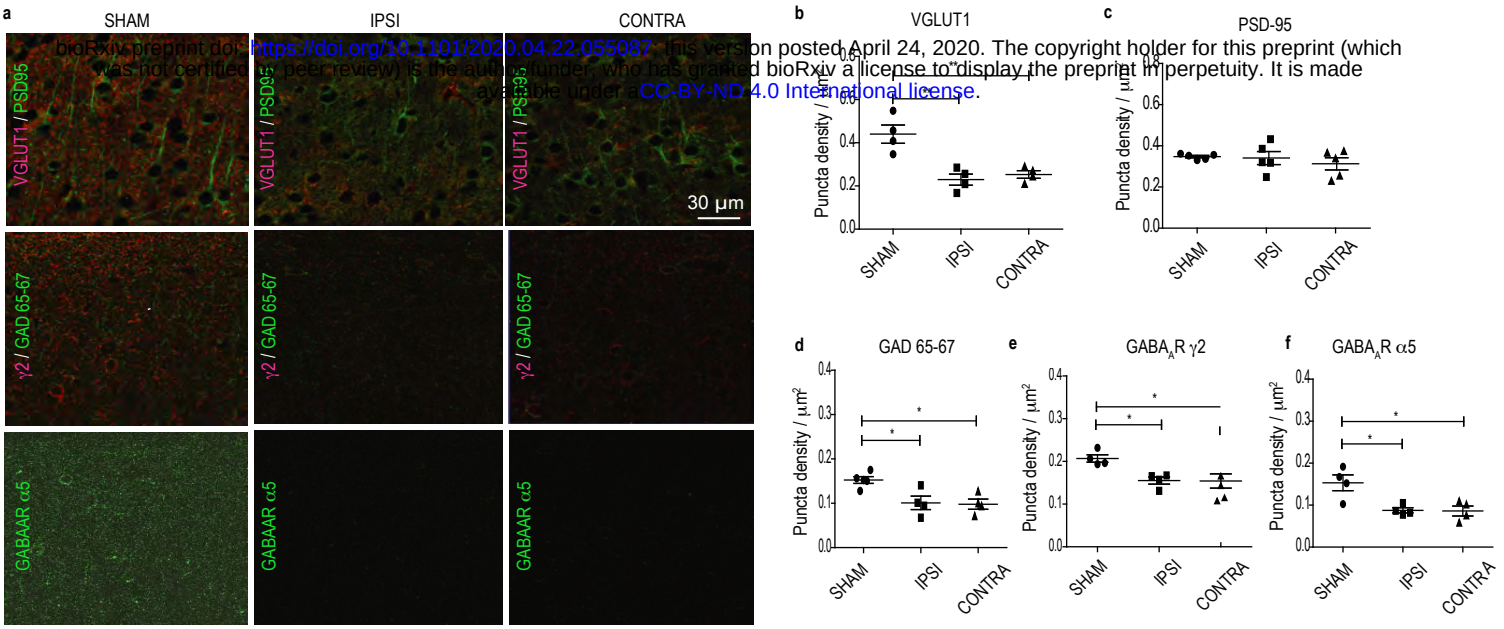

Cramer et al., Figure 5

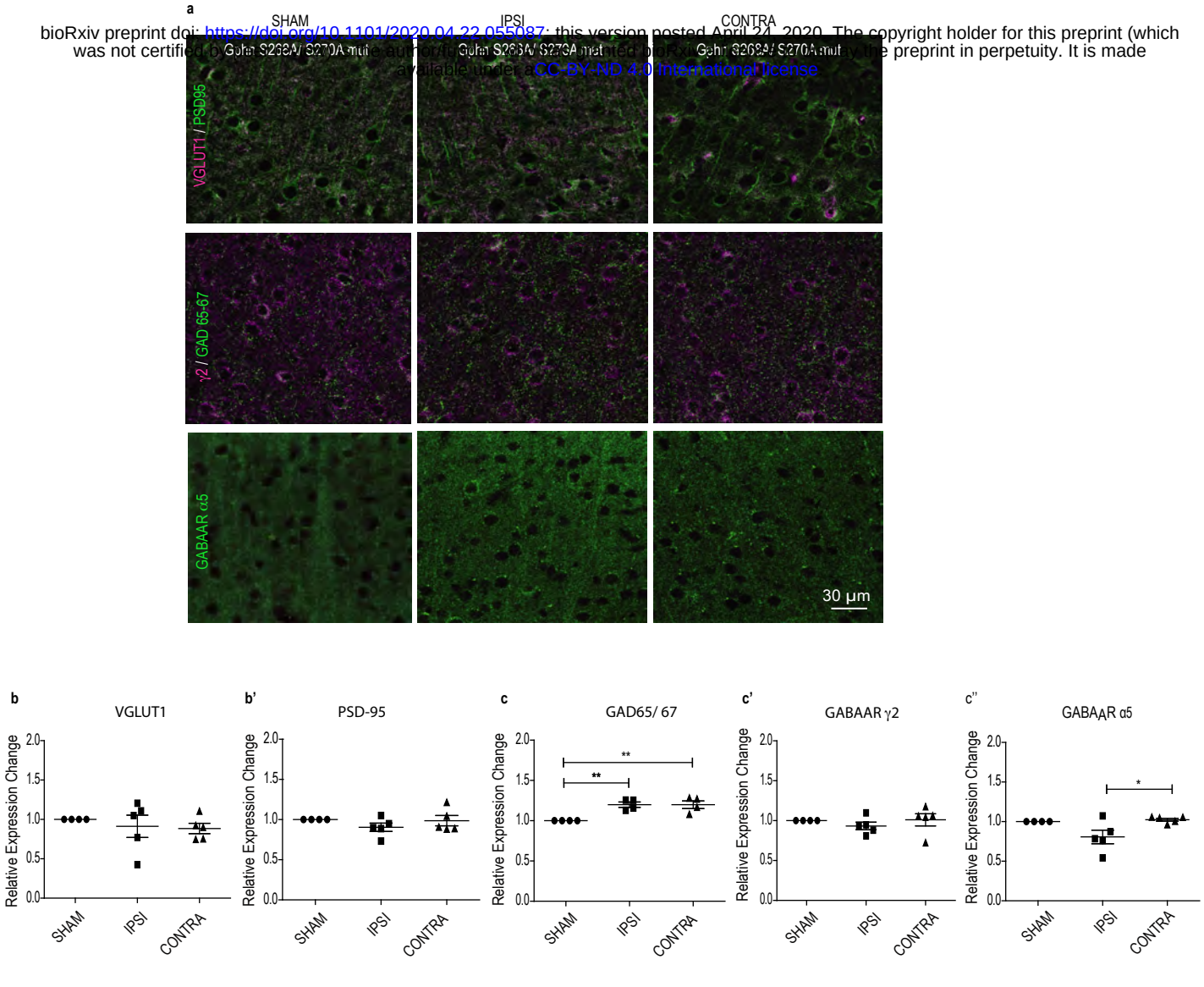

Cramer et al., Figure 6

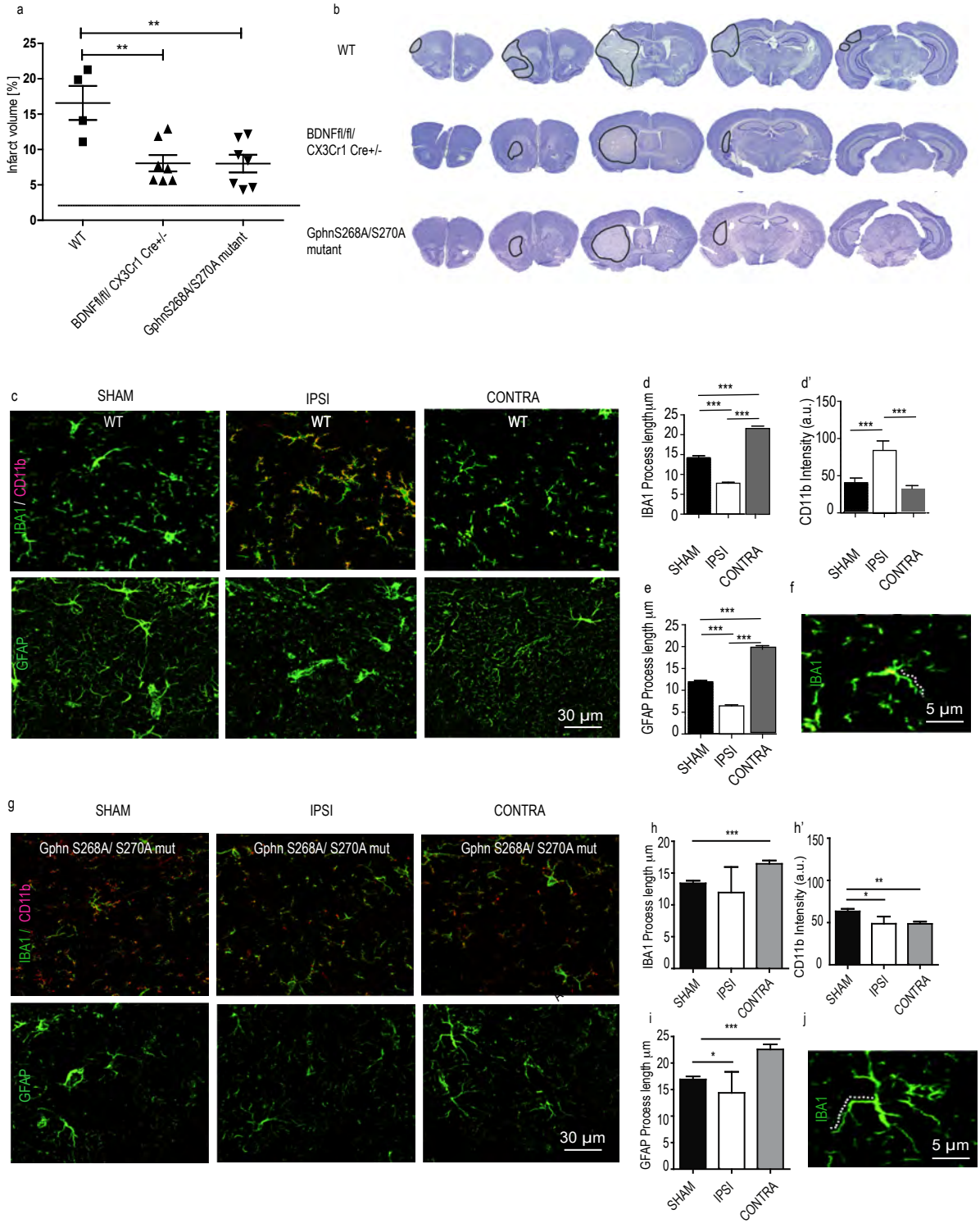

Cramer et al., Figure 7

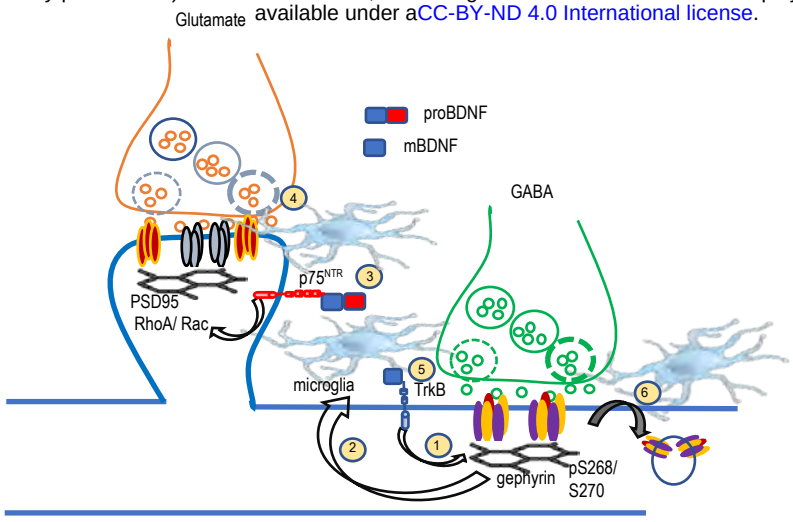

Cramer et al., Figure 8